JAMES | Journal of Advances in Modeling Earth Systems

RESEARCH ARTICLE
10.1029/2024MS004370

Advancing Organized Convection Representation in the Unified Model: Implementing and Enhancing Multiscale Coherent Structure Parameterization

Zhixiao Zhang[1], Hannah M. Christensen[1], Mark R. Muetzelfeldt[2], Tim Woollings[1], Robert S. Plant[2], Alison J. Stirling[3], Michael A. Whitall[3], Mitchell W. Moncrieff[4], Chih-Chieh Chen[4], and Zhe Feng[5]

[1]Department of Physics, University of Oxford, Oxford, UK, [2]Department of Meteorology, University of Reading, Reading, UK, [3]Met Office, Exeter, UK, [4]Climate and Global Dynamics Division, National Center for Atmospheric Research, Boulder, CO, USA, [5]Atmospheric, Climate, and Earth Sciences Division, Pacific Northwest National Laboratory, Richland, WA, USA

Abstract To address the effect of stratiform latent heating on meso- to large-scale circulations, an enhanced implementation of the Multiscale Coherent Structure Parameterization (MCSP) is developed for the Met Office Unified Model. MCSP represents the top-heavy stratiform latent heating from under-resolved organized convection in general circulation models. We couple the MCSP with a mass-flux convection scheme (CoMorph-A) to improve storm lifecycle continuity. The improved MCSP trigger is specifically designed for mixed-phase deep convective cloud, combined with a background vertical wind shear, both known to be crucial for stratiform development. We also test a cloud top temperature dependent convective-stratiform heating partitioning, in contrast to the earlier fixed partitioning. Assessments from ensemble weather forecasts and decadal simulations demonstrate that MCSP directly reduces cloud deepening and precipitation areas by moderating mesoscale circulations. Indirectly, it amends tropical precipitation biases, notably correcting dry and wet biases over India and the Indian Ocean, respectively. Remarkably, the scheme outperforms a climate model ensemble by improving seasonal precipitation cycle predictions in these regions. The scheme also improves Madden-Julian Oscillation (MJO) spectra, achieving better alignment with observational and reanalysis data by intensifying the simulated MJO over the Indian Ocean during phases 4 to 5. However, the scheme increases precipitation overestimation over the Western Pacific. Shifting from fixed to temperature-dependent convective-stratiform partitioning reduces the Pacific precipitation overestimation and further improves the seasonal cycle in India. Spatially correlated biases highlight the necessity for advances beyond deterministic approaches to align MCSP with environmental conditions.

Plain Language Summary We improve a key component of the Met Office's climate model to better represent how widespread light rain in severe convective storms affects atmospheric patterns. We make the representation respond to different temperatures at the tops of clouds, which is a new approach compared to previous studies where the heavy-to-light rain partitioning was assumed constant. We find that the improved representation of the light rain associated with severe storms reduces the overall storm rainfall area and suppresses storm height. The changes are particularly effective in correcting rainfall forecasts in tropical regions like India and the Indian Ocean, outperforming other climate models. Notably, our model excels at predicting specific tropical climate patterns, enhancing wind and rainfall accuracy over the Maritime Continent. However, our model predicts too much rain over the Western Pacific. When we adjust how we calculate the heavy-to-light rain partitioning based on cloud top temperatures, it reduces this overestimation but also weakens our improvements elsewhere. This indicates that we need to keep exploring new approaches to consider the light rain probability in severe storms.

Key Points:

- Organized convection scheme with realistic triggering and state-dependent partitioning between stratiform and convective heating is proposed
- Scheme leads to reduced storm area and shallower parameterized convection through lower-troposphere cooling from stratiform precipitation
- Scheme corrects systematic precipitation biases over India and the Indian Ocean, and also intensifies the Madden-Julian Oscillation

Supporting Information:

Supporting Information may be found in the online version of this article.

Correspondence to:

Z. Zhang,
zhixiao.zhang@physics.ox.ac.uk

Citation:

Zhang, Z., Christensen, H. M., Muetzelfeldt, M. R., Woollings, T., Plant, R. S., Stirling, A. J., et al. (2025). Advancing organized convection representation in the unified model: Implementing and enhancing multiscale coherent structure parameterization. *Journal of Advances in Modeling Earth Systems*, *17*, e2024MS004370. https://doi.org/10.1029/2024MS004370

Received 28 MAR 2024
Accepted 4 MAR 2025

Author Contributions:

Conceptualization: Zhixiao Zhang, Hannah M. Christensen, Mark R. Muetzelfeldt, Tim Woollings, Robert S. Plant, Michael A. Whitall, Mitchell W. Moncrieff
Data curation: Zhixiao Zhang
Formal analysis: Zhixiao Zhang, Hannah M. Christensen, Mark R. Muetzelfeldt, Tim Woollings, Robert S. Plant

1. Introduction

Organized convection encompasses two distinct types of precipitation: intense convective precipitation, and quasi-steady, lighter stratiform precipitation, with this differentiation observed in both tropical (Cheng & Houze, 1979) and extratropical regions (Houze et al., 1990). The variation in organized convection, encompassing a spectral mix rather than a simple spatial separation between convective and stratiform precipitation, presents a significant challenge in weather and climate prediction (Schumacher & Rasmussen, 2020), as these

Funding acquisition: Hannah M. Christensen, Tim Woollings, Robert S. Plant, Alison J. Stirling
Investigation: Zhixiao Zhang, Hannah M. Christensen
Methodology: Zhixiao Zhang, Hannah M. Christensen, Mark R. Muetzelfeldt, Tim Woollings, Robert S. Plant, Alison J. Stirling, Michael A. Whitall, Mitchell W. Moncrieff, Chih-Chieh Chen
Project administration: Hannah M. Christensen, Tim Woollings, Robert S. Plant
Resources: Tim Woollings, Robert S. Plant, Alison J. Stirling, Zhe Feng
Software: Zhixiao Zhang, Mark R. Muetzelfeldt, Robert S. Plant, Alison J. Stirling, Michael A. Whitall, Zhe Feng
Supervision: Hannah M. Christensen, Tim Woollings
Validation: Zhixiao Zhang, Hannah M. Christensen, Mark R. Muetzelfeldt, Tim Woollings
Visualization: Zhixiao Zhang, Mark R. Muetzelfeldt
Writing – original draft: Zhixiao Zhang
Writing – review & editing: Zhixiao Zhang, Hannah M. Christensen, Mark R. Muetzelfeldt, Tim Woollings, Robert S. Plant, Mitchell W. Moncrieff, Chih-Chieh Chen

precipitation types differ substantially in redistributing moisture, momentum, and heat in the atmosphere (Houze, 2004). One representative type of organized convection is a Mesoscale Convective System (MCS), which has a length scale exceeding 100 km in at least one direction (Houze, 2004).

A fundamental distinction lies in the vertical profile of latent heating. In convective regions, intense updrafts induce rapid condensation, resulting in a bottom-heavy heating profile marked by a concentration of heating in the lower and middle troposphere (Houze, 1989). Conversely, in stratiform regions, the majority of latent heating occurs higher up, usually in the upper troposphere above the freezing level (Houze, 1989). This heating aloft is predominantly driven by the deposition of vapor into ice, a process facilitated by ice hydrometeors transported from convective regions (Han et al., 2019). Additionally, most stratiform regions exhibit net latent cooling below the freezing level. This occurs because they are associated with weaker convective updrafts which lead to reduced condensate production. As a result, there is insufficient condensational heating in the lower troposphere to counteract the cooling effects of microphysical processes, such as ice melting and raindrop evaporation (Leary & Houze, 1979). These dynamical and microphysical processes collectively lead to a top-heavy heating profile in stratiform regions (Houze, 1989; Schumacher et al., 2004).

A higher ratio of stratiform to convective partitioning leads to more top-heavy latent heating, crucially reshaping large-scale atmospheric circulations (Houze, 2018). For example, satellite observations show a sharp increase in stratiform precipitation and its associated top-heavy latent heating during the active stage of the Madden-Julian Oscillation (MJO) over the Western Pacific (Barnes et al., 2015). The spatial variability of the El Niño-Southern Oscillation (ENSO) is significantly influenced by the gradient of the stratiform fraction over the Pacific (Schumacher et al., 2004). Additionally, a greater stratiform fraction aids the propagation of large-scale waves from the tropics to extra-tropical regions, a phenomenon also highlighted in the same study. Incorporating stratiform latent heating in simulations notably elevates the center of the Walker cell, enhancing its alignment with observations (Hartmann et al., 1984). Overall, the more top-heavy the latent heating profile is, the stronger the upscaling feedback becomes from organized convection to large-scale atmospheric circulations (Houze, 2018).

However, it is difficult to represent top-heavy stratiform heating in weather and climate models due to its dependence on multiscale processes (Schumacher & Rasmussen, 2020), ranging from microphysics and convective drafts to mesoscale and large-scale circulations. Climate models with coarse resolution utilizing convection parameterizations often fail to represent mesoscale circulations within organized convection (Kooperman et al., 2014). Convection-permitting models with computational grids of a few kilometers partially represent mesoscale circulations yet tend to overestimate convective precipitation (e.g., Becker et al., 2021) and updraft intensity (Varble et al., 2014a, 2014b), and underestimate stratiform fractions (Prein et al., 2020). Specifically, overly intense updrafts are too efficient in producing rimed ice and precipitating moisture in convective regions, resulting in fewer ice hydrometers aloft for feeding stratiform precipitation (Varble et al., 2014a, 2014b; Zhang et al., 2021). Even when model grid spacings reach large-eddy resolutions, the overestimation in the partitioning of convective and stratiform precipitation persists (Zhang, Varble, et al., 2024). This indicates that improving stratiform precipitation representation requires more than just better resolved dynamics. Effective representation demands a coherent paradigm that spans multiple scales.

To mitigate such biases, a promising strategy developed in past studies (Chen et al., 2021; Moncrieff, 2019; Moncrieff et al., 2017; Moncrieff & Liu, 2006) is the Multiscale Coherent Structure Parameterization (MCSP) scheme. This scheme posits that the stratiform heating aloft and lower-level cooling are directly proportional to the column-integrated convective heating estimated by a convection parameterization. The scheme is triggered in situations where strong lower-tropospheric windshear promote slantwise layer overturning, an observed feature of the classical shear-perpendicular MCS (Houze, 2004, 2018) which is treated by Lagrangian dynamical models (Moncrieff, 1992). This approach enhances global climate model representations of observed MJOs (Cao & Zhang, 2017; Chen et al., 2021; Moncrieff et al., 2017). It also improves the representation of Kelvin wave spectra and reduces mean-state bias associated with traditional convective parameterizations of tropical precipitation systems (Chen et al., 2021).

The coupling method between convection parameterization and the MCSP scheme presents opportunities for improvement. The recent implementation of MCSP by Moncrieff et al. (2017) employs the Zhang-McFarlane convection scheme (Zhang & McFarlane, 1995), using a rate of change of Convective Available Potential Energy (CAPE) threshold as the trigger for the convection scheme. However, this CAPE-based trigger can be disrupted by the introduction of stratiform aloft heating and lower-level cooling by MCSP. Such disruption may

compromise the temporal continuity of both the convection and MCSP schemes, possibly leading to intermittent or on-off behavior for either or both schemes. In addition, shallower convective systems, especially those at or below the freezing level that do not efficiently produce ice hydrometeors for stratiform precipitation, might not be associated with MCS, such that the MCSP scheme is inappropriately triggered for those cases. An improvement is needed to specifically target those deep convective systems that efficiently produce stratiform components for coupling with the MCSP scheme.

A second limitation with previous implementations of MCSP is the partitioning between stratiform and convective heating. Past studies have assumed a fixed partitioning (e.g., 50%) between stratiform and convective heating. However, this does not necessarily reflect real-world conditions, where the influence of stratiform precipitation can vary significantly due to the melting of ice hydrometeors from convection regions. A suitably varying stratiform to convective heating partitioning could offer a more realistic representation.

Aiming to progress beyond existing methods, this research is guided by the following objectives: (a) Couple the MCSP with advanced convection parameterization techniques to improve storm-lifecycle continuity and facilitate storm-track based assessment. (b) Tailor MCSP triggering conditions specifically for deep convection. (c) Develop an environmentally conditioned partitioning to effectively relate stratiform and convective heating processes. (d) Understand the scheme's direct effect in weather simulations spanning several days as well as its indirect effect in decadal simulations.

This study is carried out in the Met Office Unified Model, focusing on general circulation scales and is conducted as part of the Mesoscale Convective Systems: PRobabilistic forecasting and upscale IMpacts in the gray zonE (MCS: PRIME) project. The scheme, referred to as PRIME-MCSP, couples to a novel mass-flux convection scheme (CoMorph-A) that explicitly parameterizes convective detrainment and entrainment and smoothly transits between shallow and deep clouds (Daleu et al., 2023; Lavender et al., 2024; Whitall et al., 2022). A valuable feature of the CoMorph-A convection scheme for the current study is that it makes use of an implicit solver for its detrainment calculations. This contrasts with many other convection schemes, which can suffer from numerical overshoots and on-off behavior at the timestep level. Moreover, CoMorph-A allows convection to be initiated from any layer in the vertical, depending on the instability at each level. At least partly for these reasons, the CoMorph-A approach enhances temporal-spatial continuity of precipitation clusters, capturing storm life-cycles in the presence of the stratiform heating aloft and lower-level cooling introduced by PRIME-MCSP. This improved continuity is crucial for enabling storm tracking, facilitating the lifecycle analysis of PRIME-MCSP's effect on the internal cloud dynamics and the surrounding environments.

To evaluate the effectiveness of PRIME-MCSP, short-term weather ensemble simulations and decadal climate simulations on a global scale are both conducted. The structure of the remaining sections is as follows: Section 2 details the design of the PRIME-MCSP scheme; Section 3 describes the simulations, observations, and methodology for storm tracking; Section 4 presents an analysis of the PRIME-MCSP impact throughout the lifecycle of MCSs using short-term ensemble runs; Section 5 examines the long-term climatic impacts of the PRIME-MCSP on large-scale precipitation patterns and the MJO in decadal simulations; and Section 6 summarizes the conclusions drawn from these analyses.

2. Parameterization Scheme

The PRIME-MCSP parameterization is designed to represent the stratiform latent heating profile associated with an MCS, which is otherwise missing in models. Drawing from Moncrieff et al. (2017), Figure 1a depicts a schematic of a slantwise layer overturning pattern of wind, highlighted by the black streamlines. Additionally, the schematic shows the vertical shear of horizontal wind via straight vectors on the right, indicating a transition from westerly winds in the lower troposphere to easterly winds in the mid-troposphere. Affected by this vertical wind shear, an unstable atmospheric layer rises, culminating in a central slantwise updraft that reaches the tropopause. This principal updraft then continues horizontally as an eastward flow, with the subsequent subsidence manifesting as a mesoscale downdraft on the right, while a subsidiary branch of the updraft diverges to the left at the top.

Figure 1a presents the dynamical correspondence with microphysical processes occurring within the convective and stratiform regions. The slantwise ascending layer in the center aligns with the convective region, where condensational heating is driven by updrafts loaded with raindrops below and ice condensates starting above the

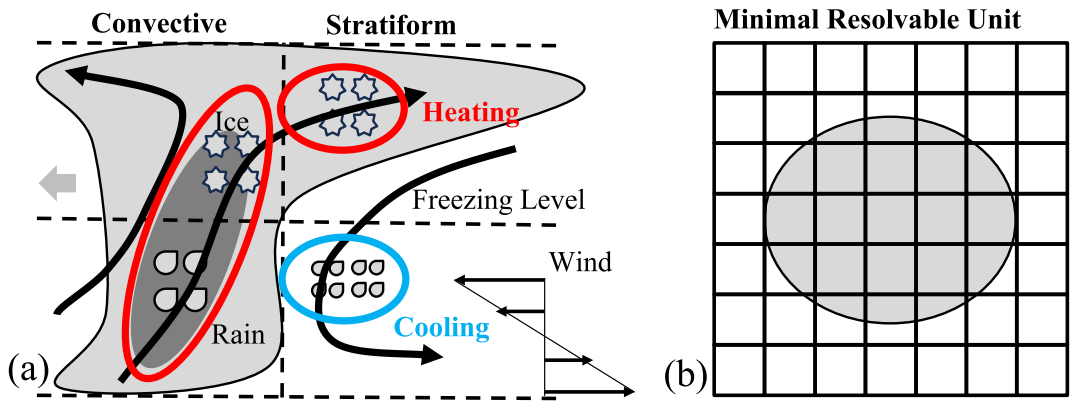

Figure 1. Schematic diagram for panel (a) stratiform and convective vertical cross sections in slantwise layer overturning scenario. Streamlines indicate wind directions. Red and blue circles represent the diabatic heating and cooling regions, respectively. The gray arrow represents the MCS propagation direction. Adapted from Moncrieff et al. (2017). (b) Top view of a 7 by 7 model-grid domain capable of minimally resolving the MCS (gray shading).

freezing level. The updrafts that curve horizontally to the right carry ice condensates aloft, aiding in the horizontal growth of the stratiform region. In the stratiform region, the ice condensates undergo depositional growth, which releases latent heat in the upper atmosphere. As these particles fall below the freezing level, they melt into raindrops. This melting process, followed by evaporation, induces cooling in the stratiform region's lower levels.

Figure 1b illustrates the MCS previously described in Figure 1a, highlighting its nature as an under-resolved phenomena for a given model resolution. Skamarock (2004) has shown that models are capable of resolving features with a minimum length scale approximately seven times the model's horizontal grid spacing. Thus, a climate model with a 100 km grid spacing could theoretically resolve MCS with a length scale of at least 700 km. However, a significant number of MCSs have at least one dimension shorter than this resolvable scale. For instance, Feng et al. (2021) demonstrated that more than 90% of MCSs over the continental United States have precipitation features shorter than 700 km, indicating a limitation in the model's ability to capture the full spectrum of MCS sizes. This complexity necessitates the use of the MCSP paradigm for multi-scale-coherent representation.

The potential temperature heating increment due to convective updrafts is parameterized by the CoMorph-A convection scheme, which has been converted to a temperature tendency and denoted as $\Delta T_{CoMorph}$. Figure 2a shows an example temperature tendency profile from the CoMorph-A scheme: this is typically a net heating effect at nearly all height levels, aligning with the conceptual model in Figure 1a.

In an advancement over previous MCSP triggers, we have formulated triggering conditions that are designed to recognize slantwise layer overturning and mixed-phase deep clouds:

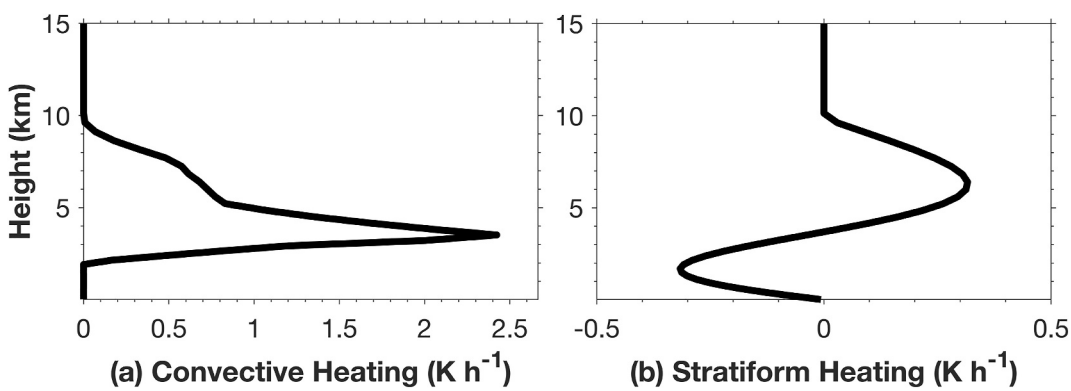

Figure 2. (a) Example tendency profile obtained from the CoMorph-A convection scheme, and (b) the corresponding stratiform tendency determined by PRIME-MCSP.

$$|\overrightarrow{V_{mid}} - \overrightarrow{V_{low}}| > 3 \text{ m s}^{-1} \quad (1)$$

$$T_{top} < 0 \text{ °C} \quad (2)$$

$$p_{base} > 600\ hPa \quad (3)$$

$$p_{base} - p_{top} > 300\ hPa \quad (4)$$

Firstly, Equation 1 identifies conditions suitable for slantwise layer overturning through the absolute value of bulk shear in the horizontal wind between 5 km ($\overrightarrow{V_{mid}}$) and 0.5 km ($\overrightarrow{V_{low}}$) above ground level. Note that Chen et al. (2021) computed only zonal wind shear when applying their triggering threshold, while this study computes wind shear based on both zonal and meridional wind components to depict the pattern of slantwise layer overturning. Secondly, the definition of mixed-phase deep cloud involves meeting three criteria, detailed in Equations 2–4: (a) The cloud top temperature (T_{top}) must be below 0°C, a threshold crucial for the production of ice condensates, which are key to generating stratiform precipitation. (b) The cloud base pressure (p_{base}) should be above 600 hPa, ensuring that there is adequate low-level moisture to support and maintain deep convection. (c) The pressure difference between the cloud base and top ($p_{base} - p_{top}$) must exceed 300 hPa, confirming that the cloud has sufficient depth.

Building on Moncrieff et al. (2017), the convective heating from CoMorph-A and the PRIME-MCSP stratiform heating are related through Equations 5–7:

$$\overline{Q_{conv}} = \frac{1}{p_s - p_{top}} \sum_{p_s}^{p_{top}} \Delta T_{CoMorph}(p)\, dp \quad (5)$$

$$Q_{strat}(p) = \alpha \sin\left(2\pi \frac{p_{top} - p}{p_s - p_{top}}\right) \overline{Q_{conv}} \quad (6)$$

$$\alpha = 0.5 \text{ or } 0.5\left(\frac{T_{freeze} - T_{top}}{T_{freeze} - T_{ref}}\right) \quad (7)$$

where p_s and p_{top} represent the surface and cloud top pressure levels, respectively, while dp denotes the pressure difference between adjacent model levels. Equation 5 calculates the column-integrated convection scheme heating from the surface to the cloud top, normalized by the total pressure difference. Equation 6 posits that the amplitude of the stratiform aloft heating is proportional to the column-integrated convective heating and to a parameter α. The sinusoidal shape means that the column integral of stratiform heating aloft and low-level cooling balances out to approximately zero. Figure 2b illustrates the vertical distribution of the emulated stratiform latent heating that corresponds to the example CoMorph-A profile of Figure 2a.

We established two separate parameterization options for the convective-stratiform heating partitioning parameter α in Equation 7. Previous studies (e.g., Chen et al., 2021) have used Equation 6 with α set to a fixed value of 0.5. Here, we also consider a variable α dependent on the temperature difference between the freezing level T_{freeze} and the cloud top T_{top}, normalized by the temperature difference between T_{freeze} and a reference cloud top level T_{ref}, as shown in Equation 7. The variable α is designed to reflect the idea that the growth of the stratiform region is proportional to the ice condensate flux from the convective to the stratiform region and that ice condensate production correlates with the temperature difference between the cloud top and the freezing level, indicated by Han et al. (2019) and Zhang, Varble, et al. (2024). T_{freeze} is set at 0°C, and T_{ref} to −80°C, representing the median value of the lifecycle-minimum cloud top temperature in global storm tracks, as guided by Feng et al. (2021).

The stratiform latent heating profile in Equation 6 is intended to have a vertical integral of zero. However, due to the discrete nature of vertical levels in the model, a small residual may exist in practice. The residual in dry static energy is computed, and used to calculate the pressure-weighted residual error, denoted as $\overline{Q_{err}}$:

Table 1
Weather Simulations Spanning From 1 July 2020, 03Z to 3 July 2020, 03Z

Name of experiment	PRIME-MCSP scheme	α	Resolution	Ensemble members
Control Run	N/A	N/A	~60 km	8
PRIME-MCSP Run	Activated	0.5	~60 km	8

$$\overline{Q_{err}} = \frac{1}{p_s - p_{top}} \sum_{p_s}^{p_{top}} Q_{strat}(p)\, dp \tag{8}$$

The final temperature tendency $\Delta T_{org}(p)$ for a given grid at a specific level, resulting from the organized convection, is computed as the sum of $\Delta T_{CoMorph}(p)$ and $Q_{strat}(p)$, adjusted by subtracting $\overline{Q_{err}}$:

$$\Delta T_{org}(p) = \Delta T_{CoMorph}(p) + Q_{strat}(p) - \overline{Q_{err}} \tag{9}$$

The PRIME-MCSP tendency as represented in Equation 9 ensures the conservation of dry static energy within a column, even after incorporating stratiform latent heating into the model. This temperature tendency is further converted back into a potential temperature tendency to integrate MCS feedback with other model components.

These equations form a simple model designed to emulate stratiform heating for sensitivity tests on the upscaling effects of MCSs. However, the scheme has several limitations. First, the use of a sinusoidal function may be overly simplistic for accurately coupling convective and stratiform heating. Second, the neutral tendency level, representing the transition from stratiform cooling to heating, is currently estimated as the midpoint between cloud top and surface pressures, but it is likely influenced by the freezing level. Similarly, the peak level of stratiform heating could also be a function of freezing level. Additionally, the assumption of cloud top in the sinusoidal function may not capture instances of convection overshoots. Furthermore, previous studies (Khouider et al., 2011; Majda & Shefter, 2001; Mapes, 2000) have shown a time lag between convective and stratiform heating due to the time required for ice hydrometeors to form and detrain, a lag that becomes more pronounced in high-resolution simulations with shorter time steps. These weaknesses should be carefully considered in future scheme development before applying it to operational scenarios.

3. Simulations, Observations, and Storm Tracking Methodology

The PRIME-MCSP scheme has been implemented into version 13.0 of the Unified Model (UM13.0), developed by the United Kingdom Met Office. Its critical modules are described in Davies et al. (2005). Both the weather ensemble and climate simulations utilize UM13.0 over a global domain. The PRIME-MCSP scheme is evaluated by comparing against control runs where PRIME-MCSP is deactivated.

The weather ensemble, as detailed in Table 1, is employed to evaluate the direct, short-term effects of PRIME-MCSP on storm lifecycles and their surrounding environments from a Lagrangian perspective. We have two ensemble groups: the control run and the PRIME-MCSP run, each consisting of eight ensemble members. The initial conditions for these ensemble members are derived from the Met Office global operational forecasts, specifically the perturbed ensemble members 1–8 from the Met Office Global and Regional Ensemble Prediction System-Global (MOGREPS-G), as detailed by Inverarity et al. (2023), and are the same for each corresponding ensemble member. Each ensemble member has a horizontal grid spacing of approximately 60 km (N216) and 70 vertical levels. The model's integration time step is 6 min. The simulations are restarted from 30 June 2020, at 21Z, and undergo a 6-hr spin-up. The analyzed simulations span a duration of 48 hr, starting from 1 July 2020, at 3Z and ending on 3 July 2020, at 3Z. Two sets of simulations are produced: a set of control runs and a set of PRIME-MCSP runs, with the latter implementing a fixed α value of 0.5. Except for the CoMorph-A convection scheme, all other physical parameterizations in these weather ensemble members align with those used in the Met Office's operational weather forecasts, as described in Bush et al. (2022).

The climate simulations, as detailed in Table 2, aim to assess the long-term effects of PRIME-MCSP on the large-scale precipitation patterns and MJO. This evaluation is based on three model runs, each spanning 20 years from September 1988 to August 2008. The simulations employ a horizontal grid spacing of approximately

Table 2
Climate Simulations Spanning September 1988 to August 2008

Name of experiment	PRIME-MCSP scheme	α	Resolution
Control Run	N/A	N/A	~135 km
PRIME-MCSP Run	Activated	0.5	~135 km
PRIME-MCSP Variable α Run	Activated	Variable α	~135 km

135 km (N96) and have 85 vertical levels. The model's integration time step is 20 min. The other model configurations follow the approach outlined by Lock et al. (2024). The set includes a control run where the PRIME-MCSP scheme is deactivated, a standard PRIME-MCSP run with a fixed α value of 0.5, and a PRIME-MCSP Variable α run. In the Variable α run, the stratiform-to-convective heating fraction is dynamically adjusted based on the cloud top temperature, as described above. Except for the adoption of the CoMorph-A convection scheme, the model setup adheres to the Met Office Atmospheric Model Intercomparison Project Phase 6 (AMIP6) configuration, with the atmospheric model being forced by climatological boundary conditions (Walters et al., 2019).

The reference data set utilized for the global assessment comprises several key sources: the Global Precipitation Climatology Project (GPCP; Adler et al., 2017), is employed to assess the accuracy of simulated monthly precipitation. Furthermore, we use 26 models from the Coupled Model Intercomparison Project Phase 6 (CMIP6; Eyring, Bony, et al., 2016) to analyze the seasonal cycle of precipitation. These 26 models were selected following the research of Lauer et al. (2023) to include only the atmospheric components of the CMIP6 models and prescribed observed SSTs. This selection, known as AMIP6, represents the state-of-the-art capability for predicting the atmospheric climate state. The NOAA Interpolated Outgoing Longwave Radiation (OLR, Liebmann & Smith, 1996) and ERA-Interim reanalysis zonal wind (Dee et al., 2011) are utilized to evaluate the MJO, ensuring consistency with the previous MCSP study (Chen et al., 2021). The observed global MCS tracks, as identified by Feng et al. (2021), are applied to assess the frequency of PRIME-MCSP scheme being called.

Customized MCS tracking technique details are listed below: We utilize the PyFLEXTRKR software, as detailed by Feng et al. (2023), employing hourly maps of Top-Of-Atmosphere (TOA) infrared brightness temperatures (IR T_b) alongside the surface rain rates. The conversion of simulated TOA OLR to IR T_b is achieved through the empirical correlation established by Yang and Slingo (2001), enabling MCS identification as depicted in Figure 3a. The MCS cold cloud shield mask is defined as its IR T_b falling below 241 K. This mask is subsequently used to estimate the rainfall area and the mean rain rate underneath the MCS.

Following Feng et al. (2021), we focus on robust MCSs with a minimum cold cloud shield size of 60,000 km^2 at the peak of their lifecycle and a duration exceeding 6 hr. Tracking a robust MCS requires a minimum 50% overlap in its cold cloud shields for two consecutive houly analysis time steps. Additional tracking configurations are elaborated in Feng et al. (2023).

Figure 3 provides an example of how the MCS tracks are matched between the control and PRIME-MCSP runs. MCS track matching between the MCS masks in the control (Figure 3a, black contours) and the corresponding PRIME-MCSP (Figure 3b, black contours) runs is performed by requiring an areal overlap ratio above 80% at the MCS initiation time. The magenta dots and lines in Figure 3a illustrate the centroids and the path of the MCS at later times within the control run. The MCS cloud region is delineated by the cold cloud shield mask, and the surrounding area of interest is defined as a region within a 600 km radius around the centroid (marked by the black circle in Figure 3a), excluding the areas under the cold cloud shield mask. The MCS cloud region and its surrounding area in the control run serve as the spatial basis ranges for computing the difference between fields in the control run and the PRIME-MCSP run. These differences are used to evaluate the effect of the PRIME-MCSP scheme throughout the MCS lifecycle.

4. Direct Effects of the Scheme in Weather Ensembles

Figure 4a shows the count of global robust MCS tracks in both control and PRIME-MCSP ensemble runs across ensemble members 1 to 8, represented by blue and green bars, respectively. The PRIME-MCSP runs show a general concurrence with the corresponding control members, albeit with a slight reduction in robust MCS track

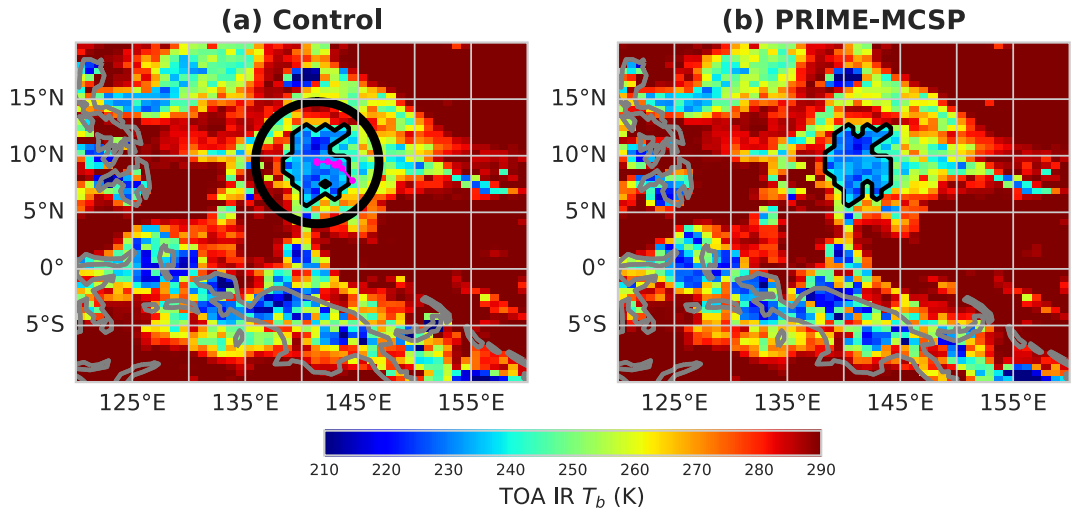

Figure 3. MCS track on 1 July 2020, at 04:00 UTC (7 hr subsequent to model initiation). (a) The control run. The magenta dots and lines trace the MCS centroids and trajectory, respectively; the circle delineates the MCS surrounding environmental area of interest. (b) The PRIME-MCSP model run. The MCS boundaries in panels (a) and (b) are delineated by black contours. The gray contours delineate the coastlines over the Maritime Continent.

numbers. The reduction in robust MCS numbers in the PRIME-MCSP runs is attributed to some convective events not meeting the minimum area requirement for defining robust MCSs due to their smaller size, as detailed later in Figure 8. Approximately one-third to one-half of MCS tracks (indicated by red bars in Figure 4a) are matchable between control and PRIME-MCSP runs, totaling 156 robust MCS tracks across 8 ensemble members. The detailed MCS track matching method has been described in Section 3.

Figure 4b shows the frequency of PRIME-MCSP scheme activations throughout the normalized MCS lifecycle. The lifecycle of the MCS is normalized into 10 timesteps, ranging from 0 (initiation) to 9 (termination). The characteristics of the MCS are linearly interpolated across these 10 normalized timesteps to facilitate the combination of lifecycle evolutions. The calling frequency is defined as the ratio between grid points activating the PRIME-MCSP scheme and the grid points within the MCS mask area. Data from all MCS tracks in ensemble members is aggregated in Figure 4b. The median MCSP frequency exhibits a relatively stable evolution throughout the lifecycle with variations from 18% to 24% of the MCS area. This is in agreement with the prior MCSP approach (e.g., Moncrieff & Liu, 2006), wherein the scheme is called in the convecting regions of the MCS, not the anvil. In addition to the combined statistics, Figure 4c shows a histogram of autocorrelation at a one-time-step lag, based on the calling frequency within each individual MCS lifecycle. The correlation coefficient is concentrated around 0.8, indicating the consistency of the calling frequency throughout each MCS lifecycle. This lifecycle continuity of calling frequency suggests effective coupling of the PRIME-MCSP scheme with the CoMorph-A convection scheme, avoiding abrupt activations or deactivations.

The PRIME-MCSP scheme primarily functions to transfer heat from the lower to the upper troposphere. We examine the evolution of spatially averaged temperature throughout the normalized lifecycles of the MCSs in both the cloud areas and surrounding environments. The normalized lifecycles, cloud areas, and MCS surrounding environments are based on the MCS tracks in the control run that have corresponding matches in the PRIME-MCSP runs. It appears that the temperature does not change much throughout the lifecycle. Therefore, our analysis focuses on the temperature differences between the PRIME-MCSP run and the control run. In Figures 5a and 5b, we observe a decrease in temperature for both the MCS cloud and the surrounding environment at 850 hPa as time progresses, with the rate of change in the MCS cloud being more pronounced. This indicates that the PRIME-MCSP scheme effectively induces cooling in the lower troposphere, as intended, and that over time, this cooling effect extends to the MCS's surrounding environment. Conversely, Figures 5c and 5d shows a general increase in temperature at 200 hPa for both the MCS cloud and the environment, again with a faster rate of change within the cloud. This demonstrates the scheme's role in upper tropospheric warming, with the additional heating in the cloud area gradually affecting the surrounding MCS environment over time.

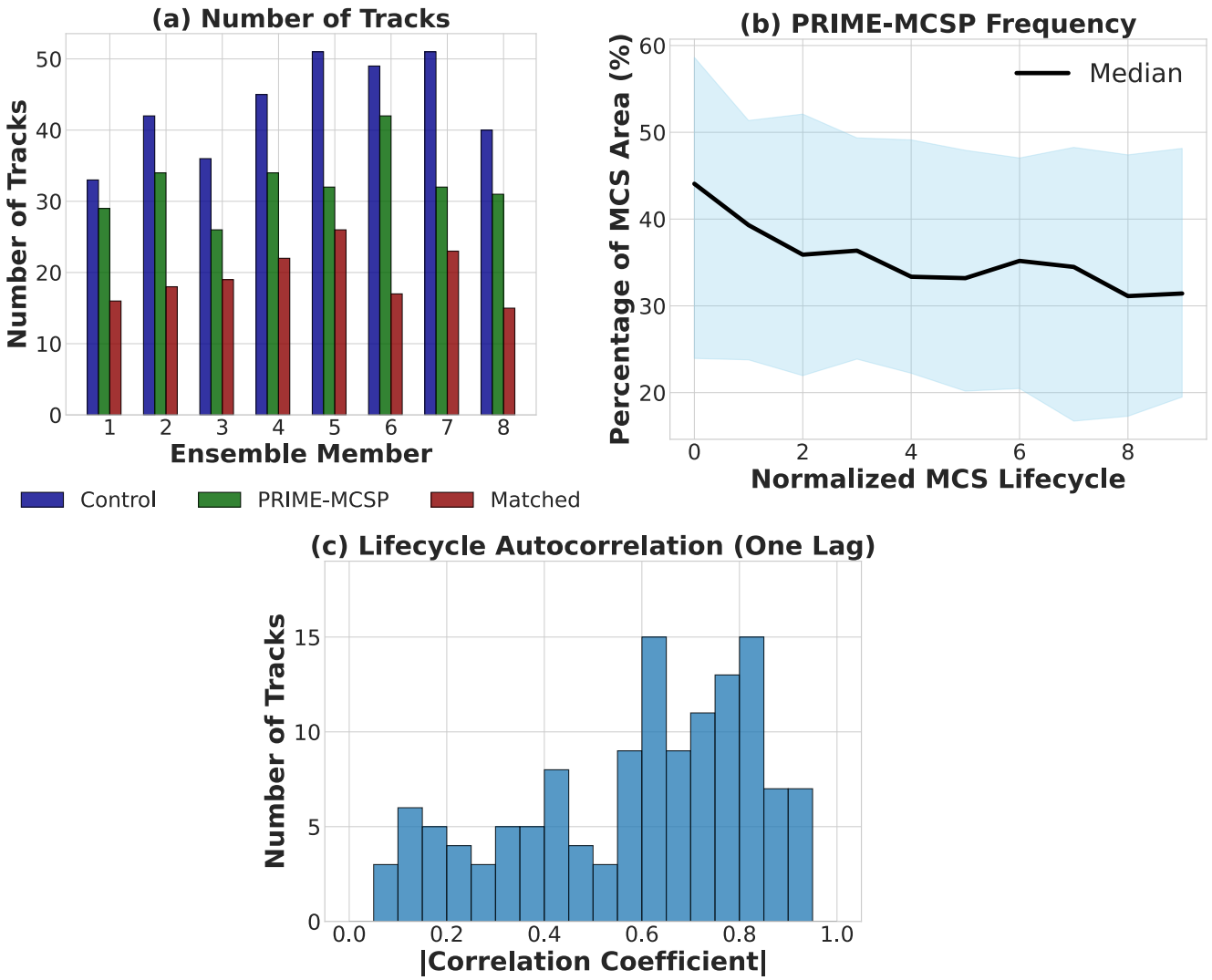

Figure 4. (a) MCS track counts, (b) invocation frequencies of the scheme across the MCS lifecycles. The shaded areas represent the Interquartile Range (IQR) in all matched tracks from all ensemble members, spanning the 25th to 75th percentiles, while the median value is depicted by the solid black line, and (c) histogram of the absolute values of MCS lifecycle autocorrelation with a one-time-step lag.

Figure 6 shows the response of 850 hPa vertical velocity to the lower tropospheric cooling induced by the PRIME-MCSP scheme. Within the MCS, a predominant positive vertical velocity is associated with ongoing convective updrafts throughout the lifecycle (Figure 6a). Conversely, in the surrounding environments of the MCS, a negative vertical velocity is also persistent, indicating the presence of environmental subsidence air (Figure 6c). When the PRIME-MCSP scheme is active, there is a weakening of convective updrafts (Figure 6b) and a corresponding weakening of the surrounding air subsidence (Figure 6d). These alterations highlight the PRIME-MCSP scheme's effect in moderating the explicit mesoscale circulations associated with the MCS. Additionally, an examination of the 200 hPa vertical velocity response (Figure S1 in Supporting Information S1) reveals no significant change, suggesting that the effects of the PRIME-MCSP upper tropospheric heating are nuanced, likely influenced by cloud top height and interactions with gravity waves.

The impact of the PRIME-MCSP scheme on regional circulation is further demonstrated in Figure 7, which presents a global map highlighting the differences in 850 hPa vertical velocity between the MCSP run ensemble mean and the control run ensemble mean. Notably, over the part of Intertropical Convergence Zone (ITCZ) between 10° and 180°W, 0°–20°N and over various extratropical low-level jet regions, the formation of three parallel bands—central blue shading flanked by two red shading bands—mirrors the findings from Figure 6,

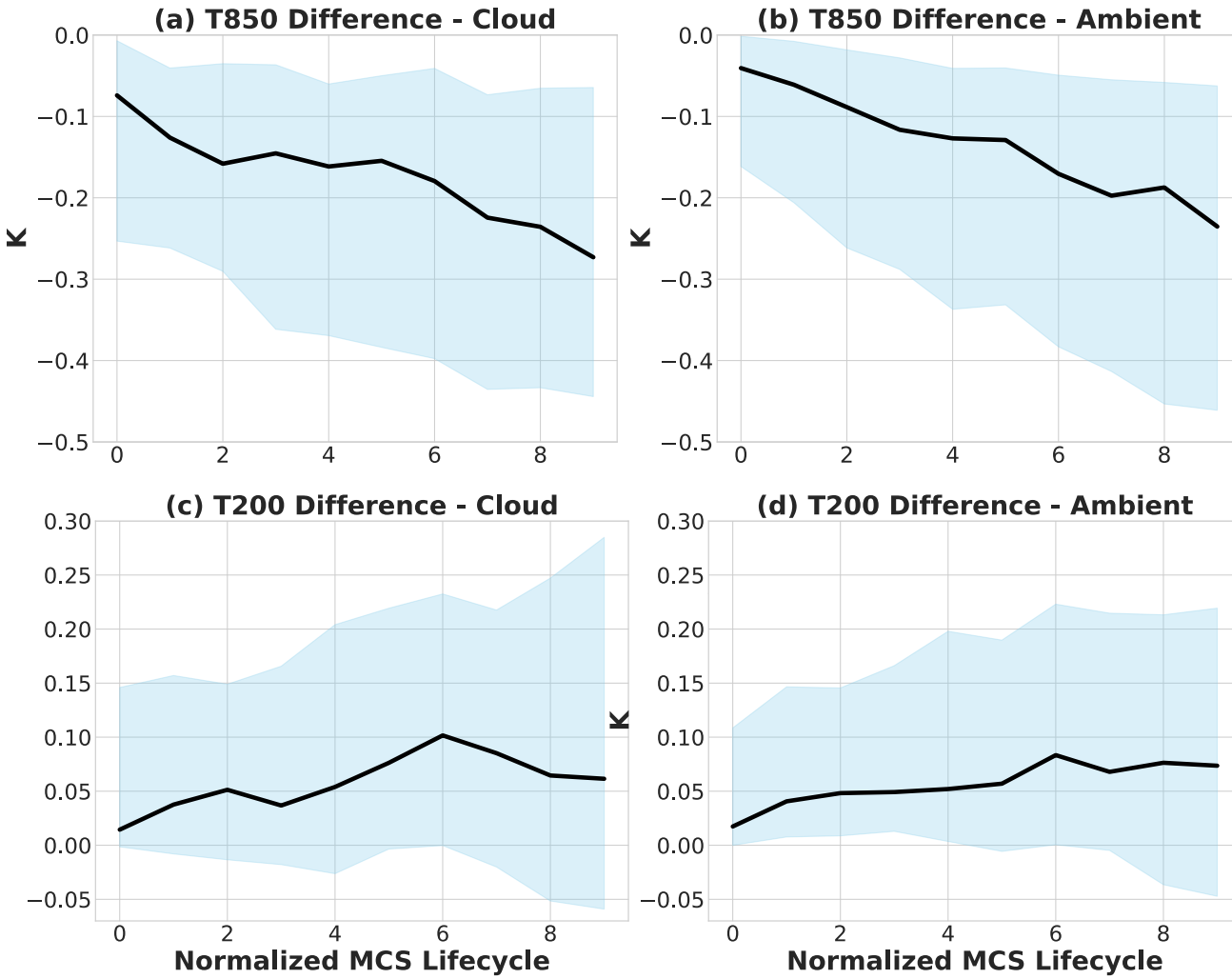

Figure 5. Temperature differences between the PRIME-MCSP and the control runs within MCS clouds and their surrounding environments at both 850 hPa (a–b) and 200 hPa (c–d) throughout the normalized MCS lifecycle, using the MCS tracks in the control run that have matches in the PRIME-MCSP runs. Shaded areas and lines follow the conventions from Figure 4b. Simulations span 1 July 2020, 03Z to 3 July 2020, 03Z.

indicating suppressed regional upward motion and reduced surrounding subsidence following the PRIME-MCSP scheme activation.

The weakened circulations are linked to changes in MCS characteristics, including convective depth, rainfall area, and rain rate. Convective depth is represented by the minimum TOA IR T_b within the MCS's cold cloud shield, where colder TOA IR T_b values signify deeper MCS convective systems (Figure 8a). The PRIME-MCSP scheme results in a consistently positive TOA IR Tb difference throughout the MCS lifecycle (Figure 8b), suggesting a reduction in convective depth. The area covered by rainfall expands as the MCS matures, stabilizing in the latter part of the lifecycle (Figure 8c). The difference in rainfall area is consistently negative (Figure 8d), indicating the PRIME-MCSP scheme's tendency to reduce the rainfall area beneath the MCS's cold cloud shield. This explains the decrease in robust MCS track numbers as shown in Figure 4a, since a reduced MCS area impacts the number of cases meeting the lifecycle-maximum area threshold. Consistent with previous research indicating a positive correlation between convective depth and MCS area (Zhang et al., 2021), the decrease in convective depth is associated here with reduction in area. The PRIME-MCSP scheme's impact on rain rate is minimal, likely because rain rate is more influenced by large-scale microphysics, and the scheme primarily modifies heating tendencies without directly affecting rain rate. Combining reduced rainfall area with an unchanged rain rate suggests a decrease in rainfall volume within MCSs following PRIME-MCSP activation.

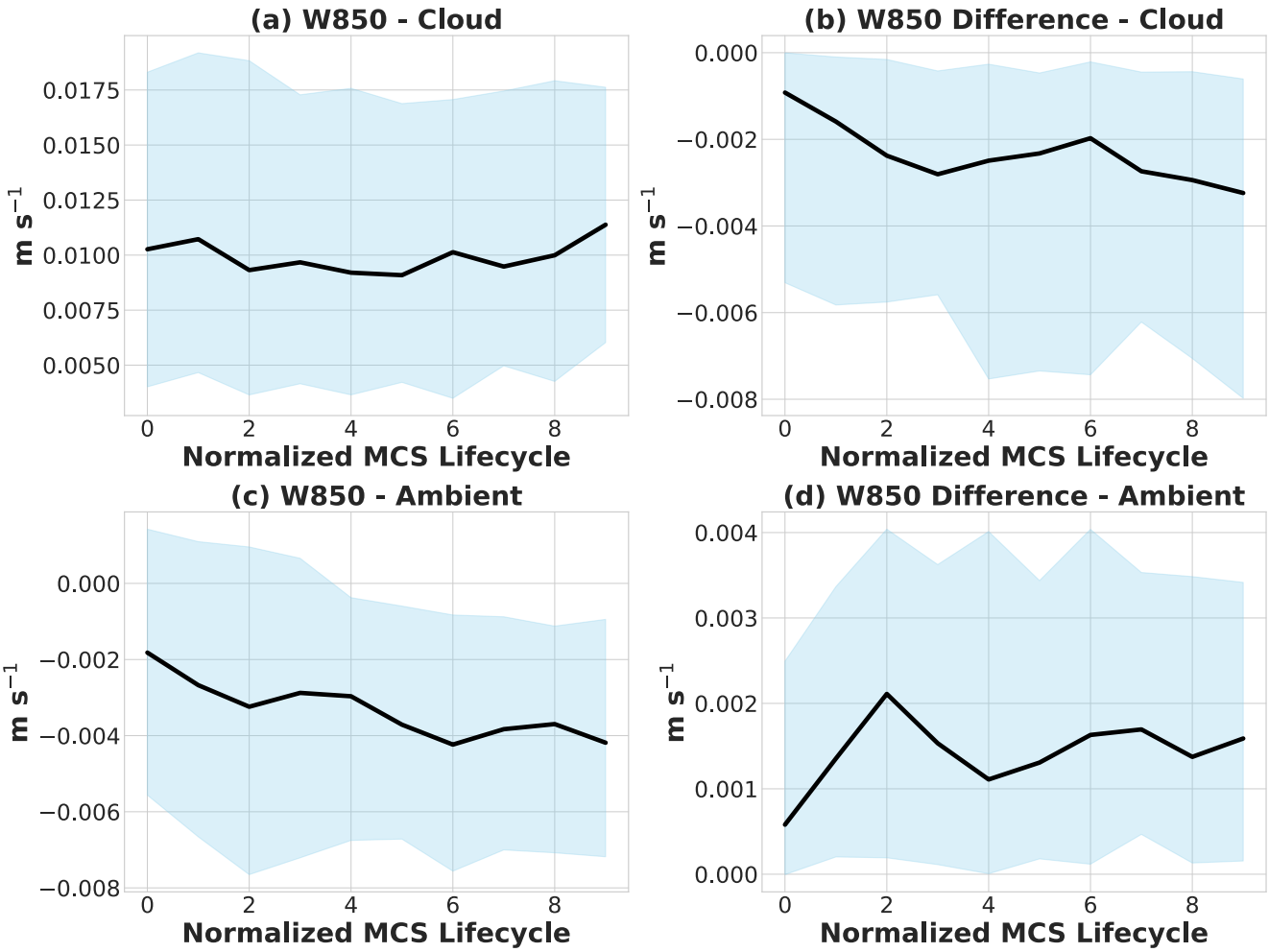

Figure 6. (a), (c) 850 hPa vertical velocity in the control runs and (b), (d) their changes following PRIME-MCSP activation, where a positive velocity indicates upward motion. Shaded areas and line conventions are as described in Figure 4b. Simulations span 1 July 2020, 03Z to 3 July 2020, 03Z.

In summary, the analysis in Figures 6–8 demonstrates the PRIME-MCSP scheme's direct impact, isolated from its long-term feedback from large-scale circulations. The initial conditions strongly constrain these short-term weather forecasts, but despite this, systematic differences do emerge, with the scheme consistently weakening mesoscale circulations in each ensemble member. However, the long-term implications of these mesoscale differences, when accumulated over time and combined with feedback from large-scale circulations, remains unclear. This motivates the assessment of the PRIME-MCSP scheme's long-term indirect effects on rainfall, as discussed in Section 5.

5. Indirect Effects of the Scheme in Decadal Simulations

Figure 9 presents a comparison of the averaged global rain rate distributions as derived from satellite retrievals (GPCP), alongside those from the control, PRIME-MCSP, and PRIME-MCSP variable α runs over a 20-year period from September 1988 to August 2008. The Pearson correlation coefficients between the GPCP and these three simulations are 0.91, 0.90, and 0.91, respectively. These correlations indicate that the PRIME-MCSP scheme maintains the accuracy of global rainfall distribution.

Figure 10a presents the difference in rainfall between the control run and GPCP retrievals, with warm and cold colors indicating precipitation overestimation and underestimation, respectively. Predominantly, the control run overestimates rainfall across most tropical regions, especially within the ITCZ. Specifically, it overestimates rainfall over the Indian Ocean and Western Pacific, while underestimating it over India and the Bay of Bengal.

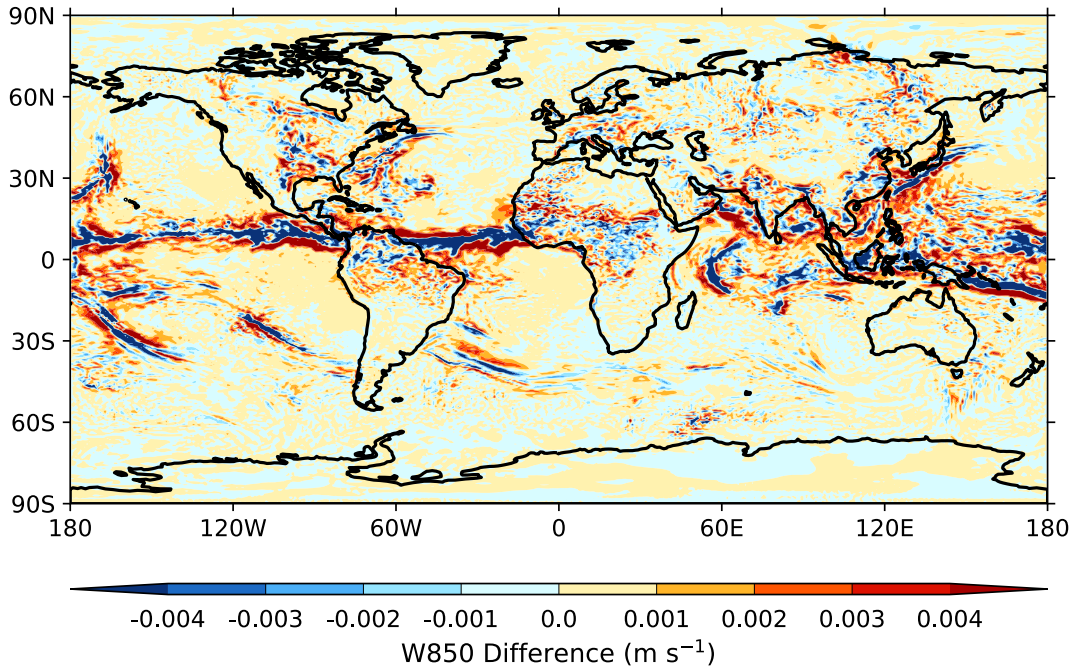

Figure 7. Ensemble mean difference in 850 hPa vertical velocity between the PRIME-MCSP and control runs, with black contours delineating coastlines. The averaging period is based on the entire 48 hr of the analyzed simulations.

These control run biases are consistent with Bush et al. (2015). Figure 10b demonstrates how PRIME-MCSP affects these biases, reversing the dry bias to a wet bias over India and mitigating the wet bias over the Indian Ocean, albeit amplifying the wet bias over the Western Pacific. The PRIME-MCSP variable α run generally agrees with the PRIME-MCSP run, with a notable reduction in the wet bias over the Western Pacific and India compared to the PRIME-MCSP run, as indicated in Figure S2 in Supporting Information S1. Overall, improvements in rainfall accuracy over India and the Indian Ocean are more pronounced in the PRIME-MCSP variable α run than the PRIME-MCSP run.

Figures 10c and 10d compare the absolute differences in rainfall biases (between the GPCP and model runs) before and after activating the PRIME-MCSP scheme, using a significance test based on 10,000 bootstrap resamples. Areas with significant changes (p values <5%) in rainfall bias are marked with stipples, with cold and warm shadings indicating bias mitigation and amplification, respectively. Both Figures 10c and 10d show dense significance stippling over India and the Indian Ocean, indicating that the improvements in these regions are statistically significant in both the PRIME-MCSP run and the PRIME-MCSP variable α run. In contrast, the PRIME-MCSP variable α run (Figure 10d) exhibits a smaller magnitude of bias change and fewer significance stipples over the Western Pacific compared to the PRIME-MCSP run (Figure 10c), suggesting better performance in the variable α run. Overall, the PRIME-MCSP variable α run outperforms the PRIME-MCSP run, as it maintains the bias reduction over India and the Indian Ocean while limiting bias amplification over the Western Pacific.

To analyze whether the precipitation bias is linked to improper triggering of the PRIME-MCSP scheme, we compared its activation frequency in the PRIME-MCSP run with real-world MCS occurrence data from June 2000 to August 2008 (Feng et al., 2021). Figure 11a shows the MCS occurrence frequency based on the observed global MCS track data set, with color shading representing the percentage of time the MCS cold cloud shield is present. Figure 11b shows the frequency of PRIME-MCSP scheme activation, defined as the percentage of timesteps during which the scheme is triggered.

MCS frequencies generally exceed PRIME-MCSP activation frequencies (compare the color scales in Figures 9a and 9b). The relative spatial patterns show general agreement but with some regional discrepancies. There is a notable disagreement over the Western Pacific, where the scheme's activation frequency shows a strong center further north than the observed MCS frequency. This aligns with the precipitation overestimation in Figure 10b, indicating that the wet bias in the Western Pacific is linked to overly frequent scheme activation. Other indirect

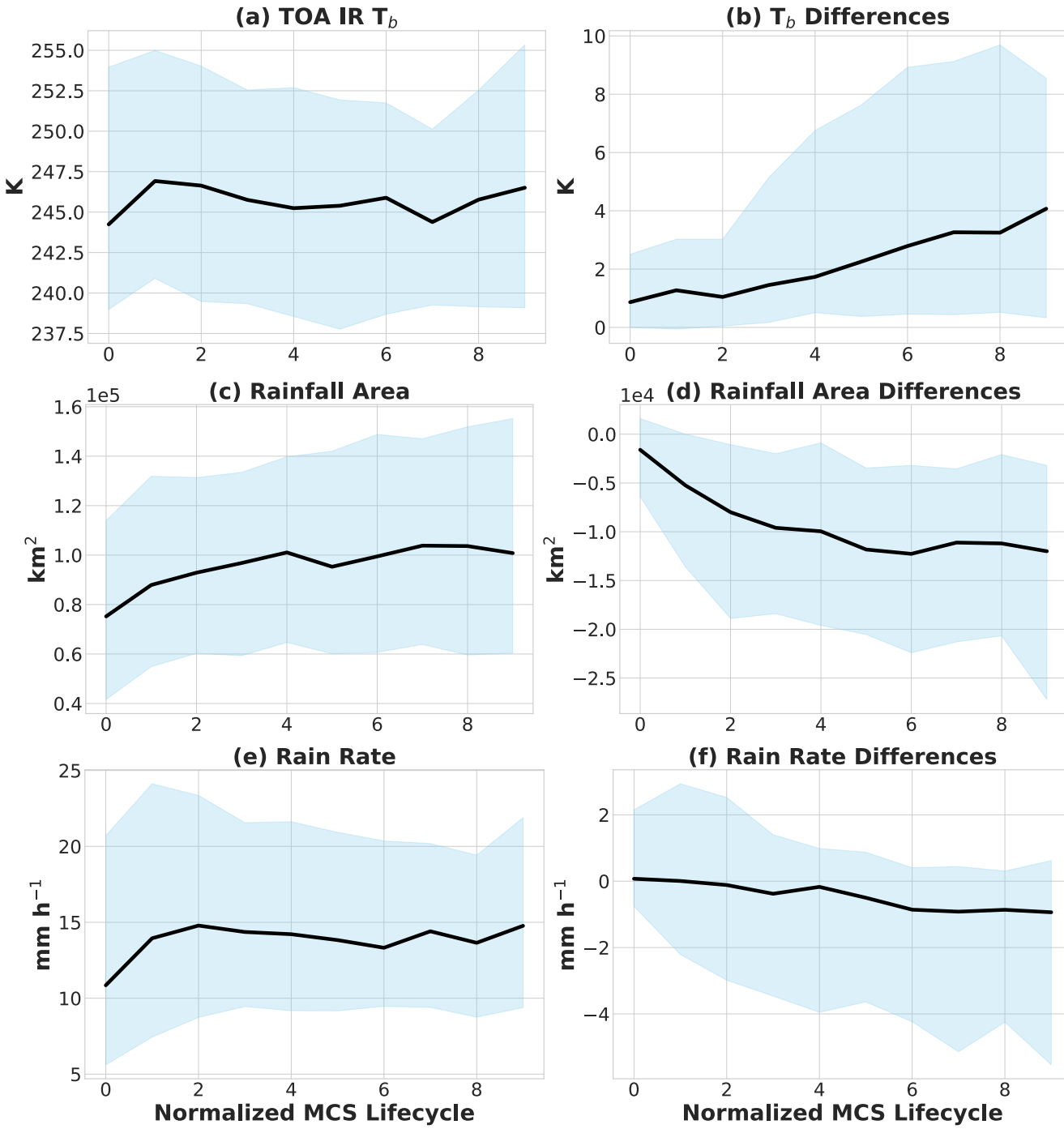

Figure 8. The lifecycles of panel (a) TOA IR T_b, (c) rainfall area, and (e) rain rate in the control run, and their changes (b, d, and f) following PRIME-MCSP activation. Simulations span 1 July 2020, 03Z to 3 July 2020, 03Z.

effects of the scheme in the Western Pacific include enhanced low-level lifting, increased cloud cover, and reduced incoming shortwave and outgoing longwave radiation, as shown in Figure S3 in Supporting Information S1. These effects may result from enhanced backscattering of kinetic energy from mesoscale to large-scale circulations, strengthening the large-scale circulation in these tropical regions.

Examining the annual precipitation cycles can offer deeper insights into the scheme's impact on the precipitation change and large scale circulations. In Figure 12, we use annual cycles to diagnose further the rainfall changes

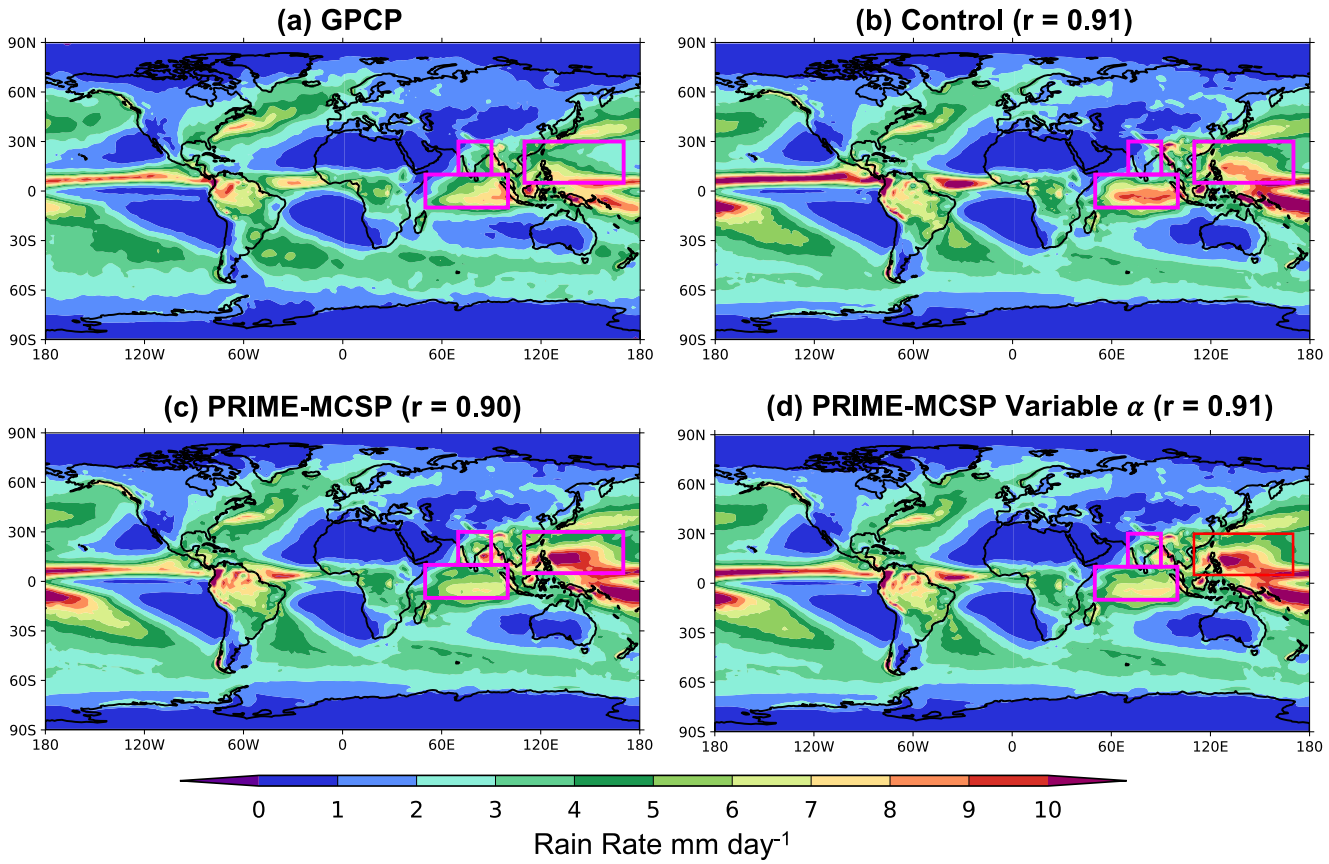

Figure 9. Average rain rate maps from panel (a) GPCP retrieval, (b) control, (c) PRIME-MCSP, and (d) PRIME-MCSP variable α runs. The Pearson correlation coefficient between the model runs and the GPCP retrieval is quoted for panels (b)–(d) as "*r*." All simulations and observations span September 1988 to August 2008. Magenta rectangles highlight regions of interest: India, the Indian Ocean, and the Western Pacific.

over India and the Indian ocean in the PRIME-MCSP run and the variable α run, comparing them with the control run and the CMIP6 ensemble simulations. The gray IQR bands reflect inter-annual variability from observations. The red IQR bands in panels (a, c, d, e, g, and h) represent inter-annual variability in UM simulations. For the CMIP6 ensemble (b and f), the red IQR combines both inter-annual variability and model-to-model variability, providing a broader measure of uncertainty across the models.

Over India, the control run significantly underestimates the rainfall, especially during the summer monsoon (Figure 12a). CMIP6 models agree better with the GPCP retrieval while overestimating the median precipitation from May to October (Figure 12b). The PRIME-MCSP run (Figure 12c) generates a higher amount of rainfall compared to the control run, though it significantly overestimates the observed rainfall amount. The PRIME-MCSP variable α run shows the closest agreement with the GPCP retrieval, outperforming the control run, the PRIME-MCSP run, and CMIP6 simulations, especially in correcting the underestimation of rainfall, as shown in Figure 12d. However, the IQRs in all these UM simulations are greater than those observed, highlighting the persistent model uncertainties across all approaches.

Over the Indian Ocean, the control run fails to capture the phase of the seasonal cycle and overestimates rainfall during all months except January (Figure 12e). CMIP6 performs better to agree with the observations in both timing and rainfall amounts from January to June, but significantly overestimates the precipitation from July to December (Figure 12f). The PRIME-MCSP run roughly captures the phase of the seasonal precipitation cycle, aligning closely with GPCP retrievals and markedly deviating from CMIP6 predictions (Figure 12g). However, it overestimates the amplitude of both the precipitation maxima and minima.

The PRIME-MCSP variable α run surpasses the PRIME-MCSP run to agree with GPCP over the Indian ocean in both phase and amplitude. It also slightly exceeds the performance of CMIP6 simulations during the winter

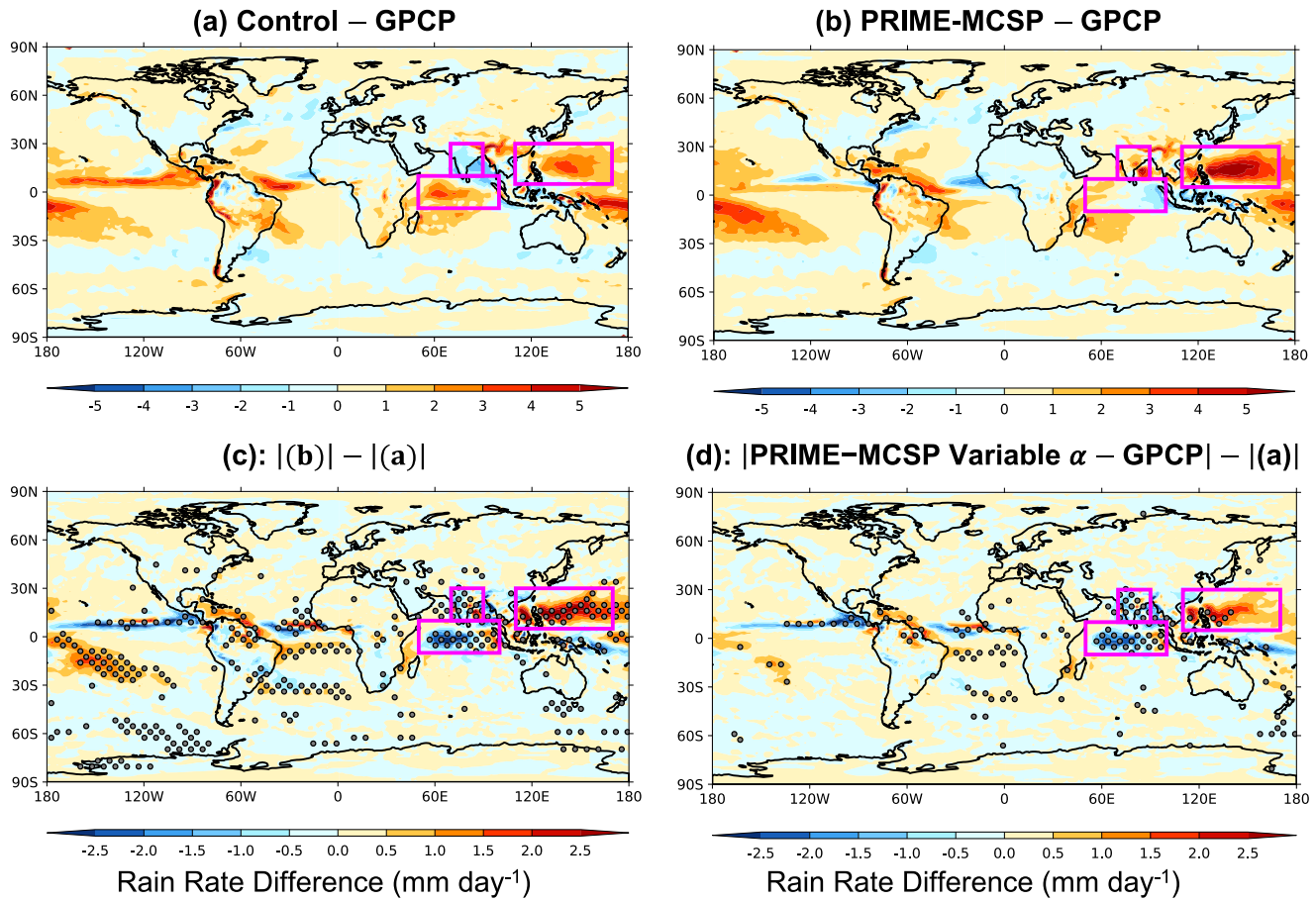

Figure 10. Rainfall difference between (a) the control run and GPCP, (b) the PRIME-MCSP run and GPCP, (c) the difference between the absolute values of (b) and (a), and (d) the same calculation as in panel (c) but for the PRIME-MCSP variable α run. The stippling in panels (c) and (d) indicates statistical significance, determined as described in the main text. Note the change of color scale between (c) and (d). All simulations and observations span September 1988 to August 2008.

months from November to March. This is particularly noteworthy given the run's coarser grid spacing relative to most CMIP6 simulations, suggesting the PRIME-MCSP scheme's upscaling effect plays a crucial role in capturing large-scale circulation patterns in this region.

The MJO plays a crucial role in influencing the annual precipitation cycle over India and the Indian Ocean, as proved in past studies (e.g., Hoell et al., 2018; Rushley et al., 2023). Although the MJO alone cannot fully explain the precipitation changes in this study, the decrease in wintertime precipitation observed in the PRIME-MCSP

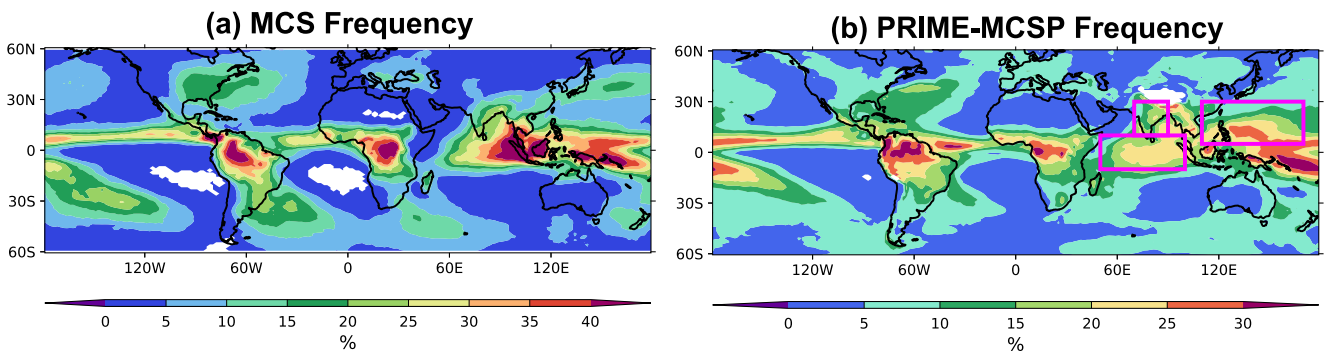

Figure 11. (a) Observed MCS occurrence frequency and (b) frequency of calling the PRIME-MCSP scheme in the decadal run. The comparison period spans June 2000 to August 2008.

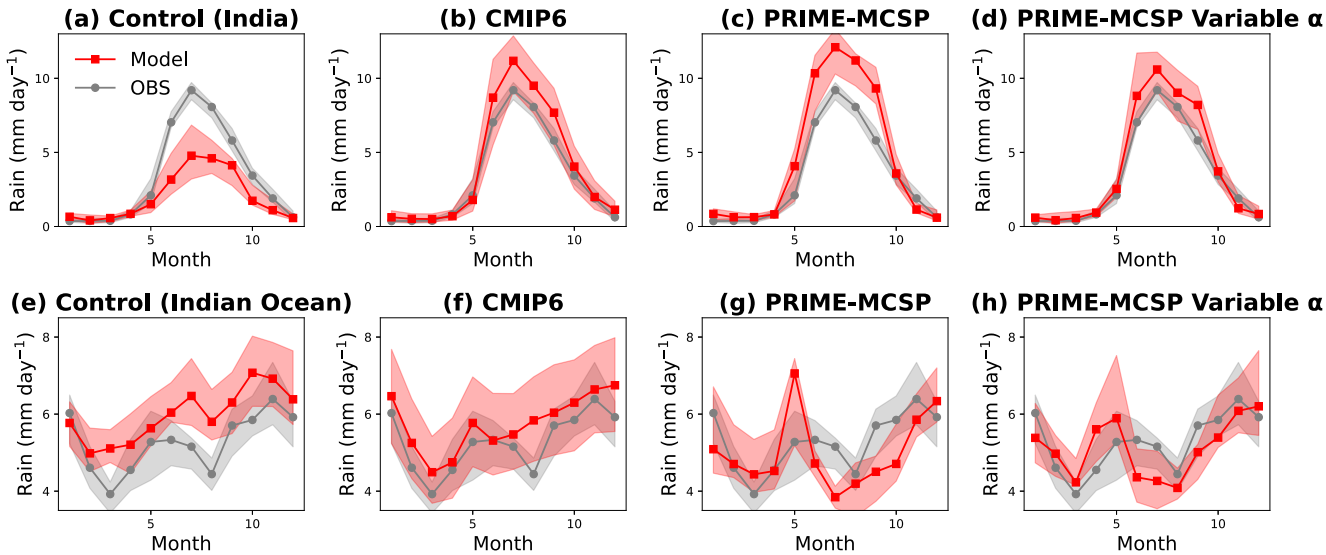

Figure 12. Simulated (red) and GPCP retrieved (gray) annual cycles of precipitation in the (a), (e) control, (b), (f) CMIP6, and (c), (g) PRIME-MCSP run, and (d), (h) PRIME-MCSP variable α run. The bands and lines indicate the IQR ranges and median values respectively. The India (a)–(d) and Indian ocean (e)–(h) regions are shown by the magenta boxes in Figure 9. All simulations and observations span from September 1988 to August 2008.

and variable α runs (Figure 12g and h vs. Figure 12e), which aligns more closely with observations and differs from CMIP6 (Figure 12f), may be associated with the improved representation of the MJO. Thus, the MJO's characteristics are analyzed for these climate runs in comparison with observations and reanalysis data, using the community software ESMValTool version 1.1.0 (Eyring, Righi, et al., 2016). The observed MJO is quatified using observed OLR and reanalysis wind, hereafter referred to as the reference data set. The simulated MJO is quantified using the corresponding variables from the simulations. The analysis focuses on a 19-year period, spanning January 1989 to December 2007, aligning with the January start month and December end month timeframe of a past study (Chen et al., 2021). These data sets have been regridded to a coarse 2.5° × 2.5° grid for fair comparison. The ESMValTool adheres to the U.S. Climate Variability and Predictability (CLIVAR) MJO Working Group's methodology (Waliser et al., 2009) for calculating wave cross spectra.

Figure 13 was generated using the ESMValTool's MJO symmetric wave cross spectra diagnostics across the latitude range of 10°N to 10°S. The coherence squared between OLR and 850-hPa zonal wind, depicted with color shading across wavenumber and frequency, highlights the presence of MJO signals. To simplify the panels, we customized the analysis by excluding vectors representing wave propagation direction and focusing the plot range on MJO-specific scales. Specifically, Figure 13a identifies a peak at the MJO's characteristic period (20–100 days) and spatial scale (wavenumbers 1–2) with an orange color shading, indicating its typical coherence squared in the reference data set. The control run's spectra display a much weaker signal in this region. Conversely, both the PRIME-MCSP and the PRIME-MCSP variable α runs generate stronger signal in this region, indicating a better alignment with the observed MJO. However, the areal coverage of the orange-shaded region in the PRIME-MCSP and PRIME-MCSP variable α runs remains smaller than that of the reference data set, indicating a persistent spectral bias between the observed and simulated MJO.

The MJO index is calculated following Wheeler and Hendon (2004) approach, which uses 10°S to 10°N averaged 850-hPa zonal wind, 200-hPa zonal wind, and OLR at the TOA. These daily fields in the reference data set, control, PRIME-MCSP, and PRIME-MCSP variable α runs are filtered to leave the 20–100 days MJO components, before they are projected onto the same multiple-variable Empirical Orthogonal Functions computed from the reference data set. Two principal components are derived to depict the east-west and north-south progression of the MJO. The magnitude of the vector formed by these components serves as the MJO index, indicating the intensity of the MJO. When the MJO index exceeds a value of 1, these components are employed to categorize data into eight MJO phases, reflecting the spatial and temporal evolution of the MJO lifecycle.

Wintertime (November to April) MJO lifecycle composite maps are shown in Figure 14, again generated by ESMValTool. These maps use darker blue shading to indicate decreases in OLR, highlighting phases of enhanced

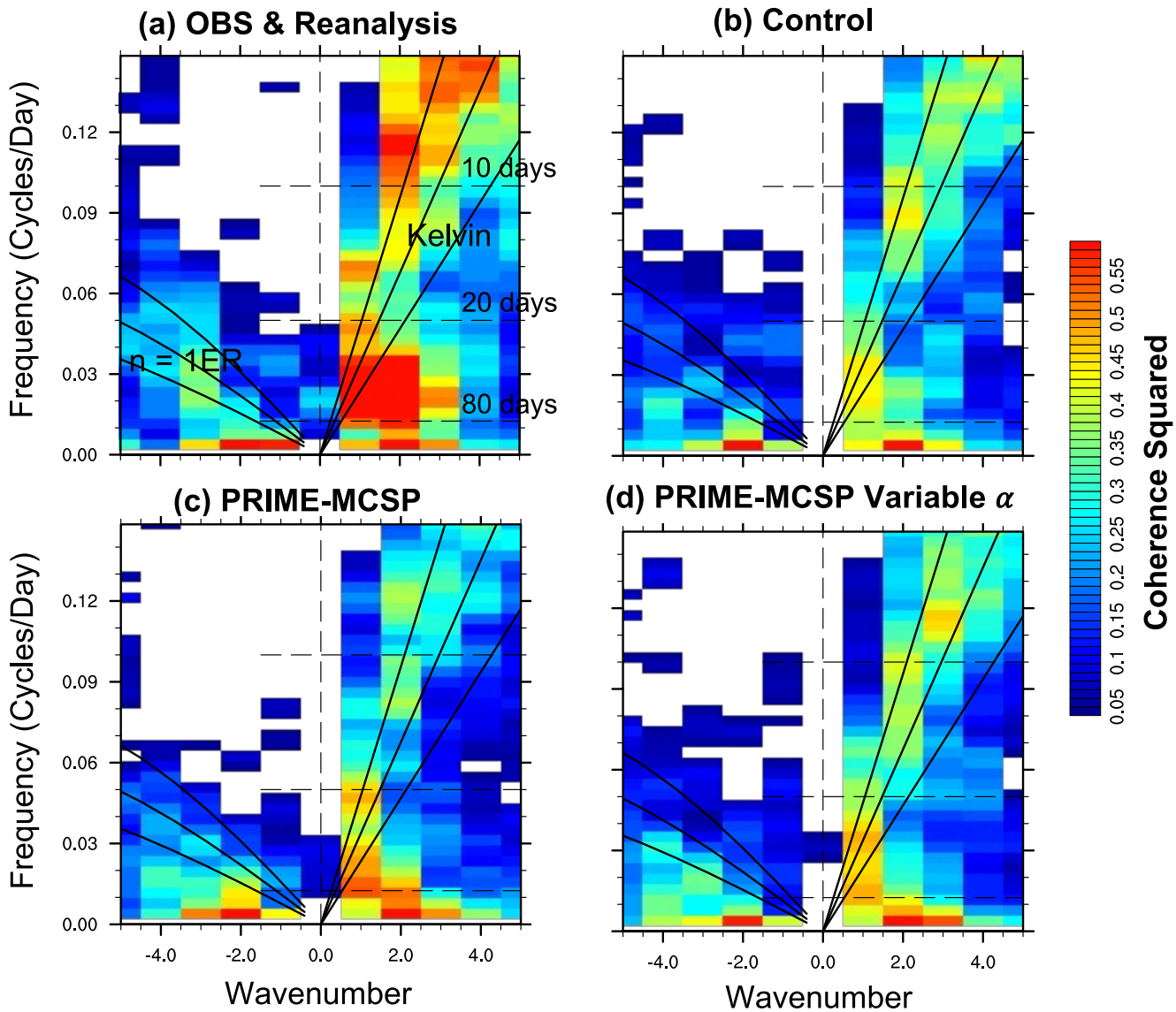

Figure 13. Coherence squared (color shading) between OLR and 850-hPa zonal wind for symmetric waves, shown across wavenumber and frequency. The dashed lines, from top to bottom, indicate wave periods of 10, 20, and 80 days, respectively. The three black lines on the left and right sides denote Equatorial Rossby (ER) waves and Kelvin waves, respectively. (a) Reference data set, (b) Control simulation, (c) PRIME-MCSP simulation, (d) PRIME-MCSP-variable-α simulation. All simulations and observations span from January 1989 to December 2007.

rainfall and large-scale upward motion associated with the MJO. The sequence from Phase 1 (P1) to Phase 8 (P8) in Figure 14a illustrates the MJO's eastward propagation through its various phases in the reference data set, with a consistent movement across the Maritime Continent. The control run (Figure 14b), however, shows discrepancies in capturing this propagation over the Indian Ocean, particularly in the absence of OLR anomalies during Phase 1 (P1) to Phase 3 (P3) and less organized patterns during Phase 4 (P4) to Phase 5 (P5) The PRIME-MCSP and PRIME-MCSP variable α runs (Figures 14c and 14d) both improve upon the control run's performance over the Indian Ocean, better capturing the observed OLR anomaly pattern during P4 to P5. This demonstrates the PRIME-MCSP scheme's effectiveness in partially improving MJO characteristics, aligning with findings from prior studies (e.g., Chen et al., 2021). The PRIME-MCSP run generates a slightly stronger OLR anomaly during Phase 3 (P3) than the PRIME-MCSP variable α run, while the PRIME-MCSP variable α run produces an OLR anomaly morphology that aligns more closely with the reference data set than the PRIME-MCSP run, suggesting sensitivity to variations of α in capturing MJO lifecycles. However, the absence of OLR anomalies during P1 to

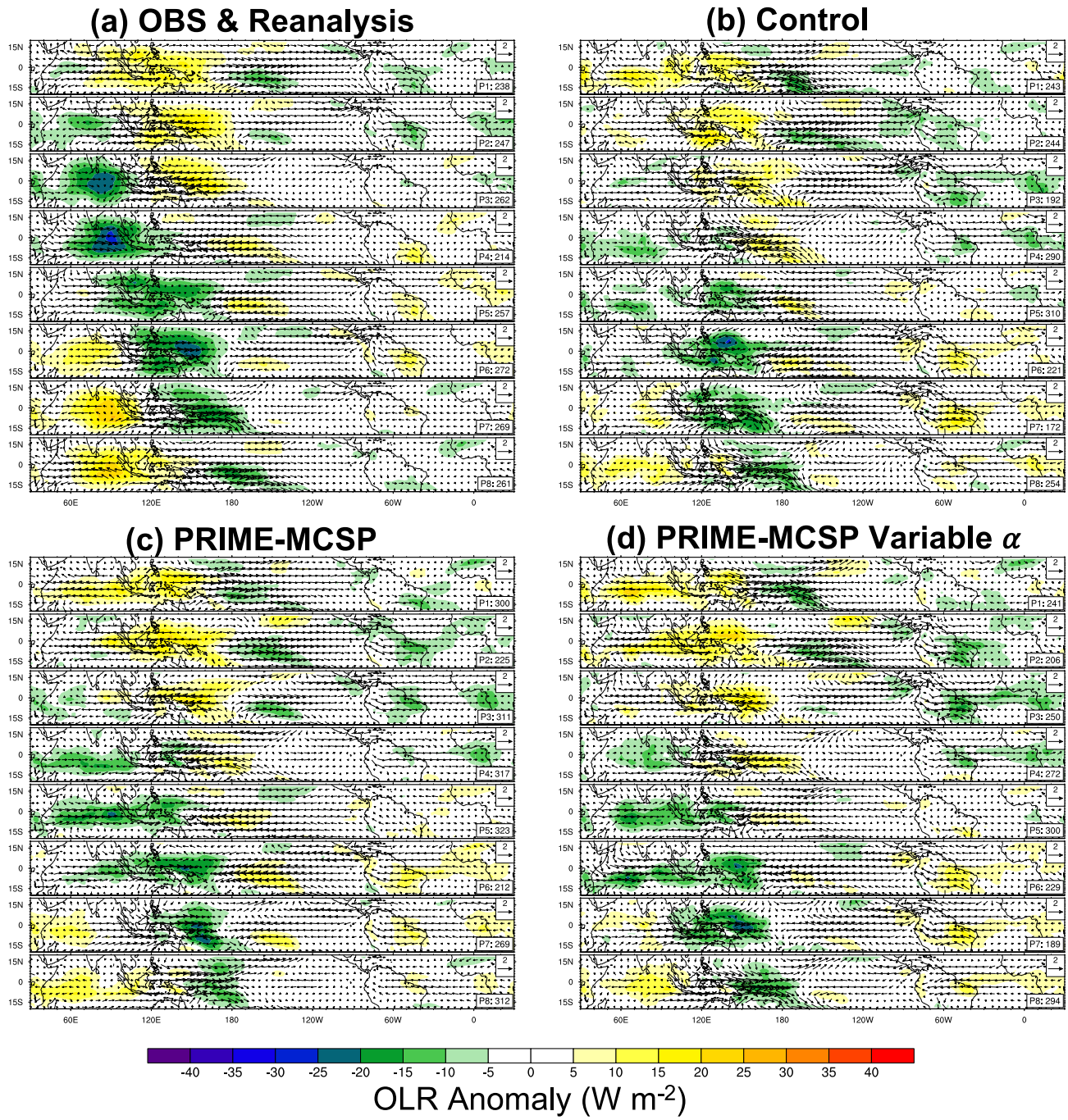

Figure 14. Wintertime (November–April) MJO lifecycle composites across different model runs: (a) Reference data set, (b) Control, (c) PRIME-MCSP, and (d) PRIME-MCSP Variable α. The color shading indicates the OLR anomalies. Wind vectors represent the 850 hPa wind field. The subpanels, labeled P1 through P8, depict the sequential phases of the MJO lifecycle and the number of days identified as that phase, used to create the composite. All simulations and observations span January 1989 to December 2007.

P3 in the simulated MJO over the Indian Ocean, compared to the observed MJO, persists across all model runs, aligning with the spectral biases highlighted in Figure 12.

To quantify differences in wintertime MJO activity across the climate runs, histogram distributions of the MJO index are analyzed. A strong MJO event is defined as having an index greater than 1. According to this definition, the number of strong MJO events can vary between the reference data set and model runs. Figure S5 in Supporting

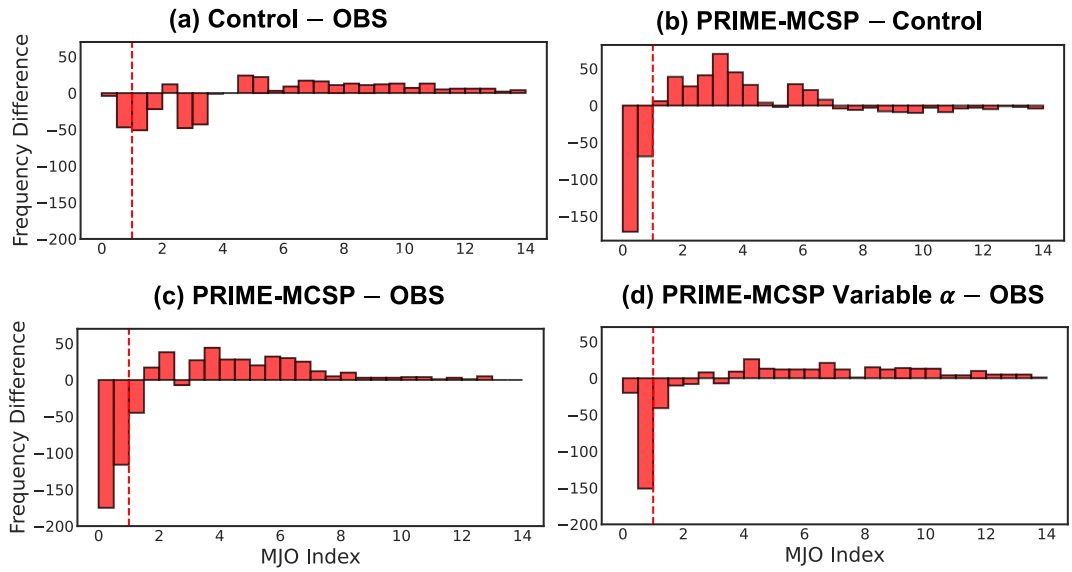

Figure 15. Comparative histogram distributions of wintertime (November–April) MJO index differences. (a) The control run against the reference data set, (b) PRIME-MCSP run versus control run, (c) PRIME-MCSP run against the reference data set, and (d) PRIME-MCSP variable α against the reference data set. The value in each bin represents the total number of MJOs that occur during the winter over the 20 years and fall within the index range.

Information S1 presents the histogram distributions of MJO indices across all data sets. The majority of MJO indices in the reference data set are below 4; however, all model runs overproduce overly strong MJO events with indices greater than 4. Figure 15 illustrates the differences in these histograms. The control run underestimates the frequency of both weak MJO events (index <1) and strong MJO events (1< index <4), while overestimating the overly strong MJO events (index >4) as shown in Figure 15a. The PRIME-MCSP run reduces the occurrence of the weaker MJO events (Figure 15b) while increasing the frequency of stronger events, mitigating the model's biases in underestimating strong MJOs. However, it also exacerbates the underestimation of weak MJO events. To assess the significance of Figure 15b, a Monte Carlo test was conducted, calculating the probability of changes in the 20-year total number of MJO occurrences between the control and the PRIME-MCSP run. This calculation was based on 100,000 resamplings using their respective annual counts of weak (index <1) and strong (index >1) MJO occurrences. The significance test revealed that the increase in strong MJO occurrences is statistically significant, with a p-value of 3.6%, well below the 5% threshold. The comparison between the PRIME-MCSP run and the reference data set (Figure 15c) shows that the PRIME-MCSP scheme shifts the model bias from underestimating strong MJOs in the control run to overestimating them. However, it may also overly suppress weak MJOs and excessively intensify the MJO. Notably, the PRIME-MCSP variable α run (Figure 15d) mitigates this over-intensification, performing the best at capturing strong MJOs (index >1) to align with the reference data set. However, the PRIME-MCSP variable α run still overly suppresses the frequency of weak MJOs compared to the control run.

6. Conclusions

This study implements the organized convection parameterization PRIME-MCSP in the Unified Model in order to represent the stratiform heating associated with MCS. The scheme incorporates several improvements over previous studies including:

(a) Specialization of MCSP triggers: The PRIME-MCSP scheme features specialized triggers for mixed-phase deep convection, incorporating ice condensate production into its determination of whether the stratiform increment should be applied. This is achieved by only triggering the scheme if the cloud top is above the freezing level. (b) Variable heating partitioning: The study explores both a constant and a variable convective-to-stratiform heating partitioning in the scheme, the latter being conditioned by cloud top temperature. (c) Leveraging the mass-flux convection parameterization: The scheme's coupling with the Comorph-A scheme is well suited to an MCS

representation because CoMorph-A has a smooth numerical behavior in time because of its allows convecting air parcels to ascend from any level, thereby promoting continuity in the MCS evolution.

The scheme's evaluation is a comprehensive analysis of both its direct effects in weather ensembles and its indirect effects in decadal simulations.

Direct effects: through an innovative use of MCS tracking, we showed that the scheme acts to suppress MCS deepening and reduce MCS precipitation area. This is attributed to the weakening of low-level mesoscale circulations associated with suppressed convective updrafts in response to the stratiform lower-tropospheric cooling.

Indirect Effects: 20-year climate simulations assess the scheme's long-term impact, exhibiting a general agreement with global observed MCS frequencies, with regional variations over the tropical regions. Key results include (a) a reduction in precipitation bias across the Maritime time continent, effectively mitigating the dry bias over India and wet bias over the Indian Ocean; (b) The precipitation bias reduction is associated with a significant improvement in the representation of the wintertime precipitation over the Indian and Indian Ocean, correcting a systematic bias observed across CMIP6 ensemble members; and (c) The scheme improves MJO spectra, aligning more closely with the observed MJO by enhancing MJO intensity over the Indian Ocean.

The improvements of the PRIME-MCSP scheme at representing the MJO and tropical precipitation are consistent with past studies while offering new insights into their sensitivity to variable heating partitioning. Boyle et al. (2015) found that MJO variability is sensitive to deep convection parameterization, with improvements linked to a higher lateral entrainment rate and reduced precipitation efficiency, which aligns with PRIME-MCSP's effect in weakening upward motion and reducing precipitation within MCSs. The intensification of the MJO by MCS stratiform latent heating is consistent with past studies (e.g., Cao & Zhang, 2017; Chen et al., 2021). However, the MJO index quantitative analysis in this study reveals that the scheme may overly intensify strong MJOs while suppressing weak MJOs within this Met Office UM setup. Introducing variable stratiform heating conditioned by cloud-top characteristics shows promise in mitigating the scheme's tendency to over-intensify the MJO, potentially resulting in a better alignment with observations.

Despite these advances, the scheme's tendency to overestimate precipitation over the Western Pacific and overly suppress weak MJOs presents an ongoing challenge and reflects limitations observed in previous MCSP implementations (e.g., Moncrieff, 2019). The implementations of MCSP in climate models are presently focused on shear-perpendicular systems with particular attention to the well-known classical MCS. Liu and Moncrieff (2017) showed that organized systems over the Western Pacific are often oriented parallel to lower-tropospheric windshear. Broadly similar convective systems are known to populate the ITCZ (Dudhia & Moncrieff, 1987; Khouider & Moncrieff, 2015). The MCSP paradigm is capable of addressing these systems by using distinct transport properties for shear-parallel systems salient to deep and shallow convection (Moncrieff, 1981). The thermodynamic properties of shear-perpendicular and shear-parallel systems are broadly similar, but momentum transport properties differ enormously. Specifically, shear-parallel systems slant downshear distinct from the upshear slant of the MCS. Consequently, momentum transport by these two organizational categories have opposite sign, and their vertical profiles differ substantially. These structural and transport characteristics may be considered the deep convection counterpart of the Grubišić and Moncrieff (2000) treatment of shallow shear-parallel cloud bands in midlatitude polar outbreaks which are remarkably analogous to trade-wind cloud streets in the tropics.

Additionally, the exploration of variable convective and stratiform partitioning proved to be a successful bias mitigation strategy over the Western Pacific while maintaining the improved precipitation representation over India and the Indian Ocean. Notably, Khouider et al. (2023) suggested that stochastic parameterization could potentially improve the representation of convective organization by refining the predicted mass flux of convective updrafts. This presents intriguing possibilities for future investigations into the stochastic parameterization of MCSP triggering and convective-to-stratiform partitioning probabilities, conditioned by various environmental patterns (Muetzelfeldt et al., 2025), which might further reduce the Western Pacific's wet bias while maintaining the desirable improvements to seasonal precipitation predictability over India and the Indian Ocean. Additionaly, future quantitative development could benefit from applying eigenmode decomposition of heating profiles (Ajayamohan et al., 2016; Deng et al., 2016; Kassahari & Puri, 2020; Khouider et al., 2011) in climate simulations and analysis data sets, as well as analyzing satellite-derived heating profile retrievals and analysis increments from data assimilation cycles. These approaches could aid in building a more sophisticated

function to couple convective and stratiform heating, incorporating the potential time lag as a fuction of environmental conditions.

Adapting this parameterization to make it scale-aware for varying model resolutions presents notable challenges. For MCS stratiform regions, which typically range from 100 to 1,000 km, grid spacings finer than 14–140 km are required to resolve them, as the minimum resolved scale is seven times the grid spacing (Skamarock, 2004). Thus, a wide range of resolutions fall into the gray zone, where stratiform structures are only partially resolved. Additionally, MCS stratiform heating is influenced by multiscale interactions, ranging from convective drafts (several kilometers) to microphysical processes at even smaller scales (Houze, 2004). As a result, even convection-permitting models with grid spacings of several kilometers cannot fully resolve stratiform heating (e.g., Zhang, Varble, et al., 2024). This indicates that the PRIME-MCSP scheme will remain relevant as model resolution increases. However, it is unclear what proportion of stratiform heating remains under-resolved at finer resolutions. Evidence from past studies (e.g., Moncrieff & Liu, 2006) does suggest that parameterized MCSs become weaker at higher resolutions, indicating that these models may increasingly resolve more MCS stratiform components. This underscores the need for caution to avoid double counting stratiform heating when applying this parameterization in high-resolution models. To address this, future work is needed to develop scale-aware parameterizations by quantifying how under-resolved and resolved stratiform components vary with model resolution.

Data Availability Statement

The source code for the PRIME-MCSP parameterization scheme is provided by Zhang, Christensen, et al. (2024). Monthly global precipitation data are supplied by the Global Precipitation Climatology Project (GPCP), as detailed by Adler et al. (2017). CMIP6 simulated precipitation data sets are provided by Eyring, Bony, et al. (2016). MCS tracks are generated using the PyFLEXTRKR software, provided by Feng et al. (2023). The MCS tracking setup for PyFLEXTRKR has been uploaded to Zenodo by Zhang et al. (2025). The supporting data sets for this study, also available on Zenodo by Zhang et al. (2025), include those used in the MJO analysis, the monthly mean precipitation from decadal climate simulations, and key variables from short-term weather ensemble runs.

Acknowledgments

This research is supported by the UK Research and Innovation (UKRI) Natural Environment Research Council (NERC) Grant NE/W005530/1 "Mesoscale Convective Systems: PRobabilistic forecasting and upscale IMpacts in the grey zonE (MCS: PRIME)." HMC was also funded by NERC Grant NE/P018238/1 and through a Leverhulme Trust Research Leadership Award. Weather ensemble runs and decadal climate simulations were performed on the Monsoon2, a joint supercomputer system of the Met Office and NERC. Scheme assessments were carried out on the JASMIN UK high-performance computing clusters, funded by the Science and Technology Facilities Council on behalf of NERC. We sincerely thank the two anonymous reviewers and the editors for their insightful comments and suggestions, which have significantly improved the manuscript. We extend our gratitude to Dr. Anne McCabe and Dr. Adrian Lock from the UK Met Office for their invaluable support in providing the necessary setup to conduct the Unified Model runs.

References

Adler, R., Wang, J.-J., Sapiano, M., Huffman, G., Bolvin, D., Nelkin, E., & NOAA CDR Program. (2017). Global Precipitation Climatology Project (GPCP) Climate Data Record (CDR), version 1.3 (Daily) [Dataset]. *NOAA National Centers for Environmental Information*. https://doi.org/10.7289/V5RX998Z

Ajayamohan, R. S., Khouider, B., Majda, A. J., & Deng, Q. (2016). Role of stratiform heating on the organization of convection over the monsoon trough. *Climate Dynamics*, *47*(12), 3641–3660. https://doi.org/10.1007/s00382-016-3033-7

Barnes, H. C., Zuluaga, M. D., & Houze, R. A., Jr. (2015). Latent heating characteristics of the MJO computed from TRMM observations. *Journal of Geophysical Research: Atmospheres*, *120*(4), 1322–1334. https://doi.org/10.1002/2014JD022530

Becker, T., Bechtold, P., & Sandu, I. (2021). Characteristics of convective precipitation over tropical Africa in storm-resolving global simulations. *Quarterly Journal of the Royal Meteorological Society*, *147*(741), 4388–4407. https://doi.org/10.1002/qj.4185

Boyle, J. S., Klein, S. A., Lucas, D. D., Ma, H.-Y., Tannahill, J., & Xie, S. (2015). The parametric sensitivity of CAM5's MJO. *Journal of Geophysical Research: Atmospheres*, *120*(4), 1424–1444. https://doi.org/10.1002/2014JD022507

Bush, M., Boutle, I., Edwards, J., Finnenkoetter, A., Franklin, C., Hanley, K., et al. (2022). The second met office unified model/jules regional atmosphere and land configuration, RAL2. *Geoscientific Model Development Discussions*, *2022*, 1–35. https://doi.org/10.5194/gmd-2022-209

Bush, S. J., Turner, A. G., Woolnough, S. J., Martin, G. M., & Klingaman, N. P. (2015). The effect of increased convective entrainment on Asian monsoon biases in the MetUM general circulation model. *Quarterly Journal of the Royal Meteorological Society*, *141*(686), 311–326. https://doi.org/10.1002/qj.2371

Cao, G., & Zhang, G. J. (2017). Role of vertical structure of convective heating in MJO simulation in NCAR CAM 5.3. *Journal of Climate*, *30*(18), 7423–7439. https://doi.org/10.1175/JCLI-D-16-0913.1

Chen, C. C., Richter, J. H., Liu, C., Moncrieff, M. W., Tang, Q., Lin, W., et al. (2021). Effects of organized convection parameterization on the MJO and precipitation in E3SMv1. Part I: Mesoscale heating. *Journal of Advances in Modeling Earth Systems*, *13*(6). https://doi.org/10.1029/2020MS002401

Cheng, C. P., & Houze, R. A. (1979). The distribution of convective and mesoscale precipitation in GATE radar echo patterns. *Monthly Weather Review*, *107*(10), 1370–1381. https://doi.org/10.1175/1520-0493(1979)107<1370:TDOCAM>2.0.CO;2

Daleu, C. L., Plant, R. S., Stirling, A. J., & Whitall, M. (2023). Evaluating the CoMorph-A parametrization using idealized simulations of the two-way coupling between convection and large-scale dynamics. *Quarterly Journal of the Royal Meteorological Society*, *149*(757), 3087–3109. https://doi.org/10.1002/qj.4547

Davies, T., Cullen, M. J. P., Malcolm, A. J., Mawson, M. H., Staniforth, A., White, A. A., & Wood, N. (2005). A new dynamical core for the Met Office's global and regional modelling of the atmosphere. *Quarterly Journal of the Royal Meteorological Society*, *131*(608), 1759–1782. https://doi.org/10.1256/qj.04.101

Dee, D. P., Uppala, S. M., Simmons, A. J., Berrisford, P., Poli, P., Kobayashi, S., et al. (2011). The ERA-interim reanalysis: Configuration and performance of the data assimilation system. *Quarterly Journal of the Royal Meteorological Society*, *137*(656), 553–597. https://doi.org/10.1002/qj.828

Deng, Q., Khouider, B., Majda, A., & Ajayamohan, R. (2016). Effect of stratiform heating on the planetary-scale organization of tropical convection. *Journal of the Atmospheric Sciences*, *73*(1), 371–392. https://doi.org/10.1175/JAS-D-15-0178.1

Dudhia, J., & Moncrieff, W. W. (1987). A numerical simulation of quasi-stationary tropical bands. *Quarterly Journal of the Royal Meteorological Society*, *113*(477), 929–967. https://doi.org/10.1002/qj.49711347711

Eyring, V., Bony, S., Meehl, G. A., Senior, C. A., Stevens, B., Stouffer, R. J., & Taylor, K. E. (2016). Overview of the Coupled Model Intercomparison Project Phase 6 (CMIP6) experimental design and organization. *Geoscientific Model Development*, *9*(5), 1937–1958. https://doi.org/10.5194/gmd-9-1937-2016

Eyring, V., Righi, M., Lauer, A., Evaldsson, M., Wenzel, S., Jones, C., et al. (2016). ESMValTool (v1.0)—A community diagnostic and performance metrics tool for routine evaluation of Earth system models in CMIP. *Geoscientific Model Development*, *9*(5), 1747–1802. https://doi.org/10.5194/gmd-9-1747-2016

Feng, Z., Hardin, J., Barnes, H. C., Li, J., Leung, L. R., Varble, A., & Zhang, Z. (2023). PyFLEXTRKR: A flexible feature tracking Python software for convective cloud analysis. *Geoscientific Model Development*, *16*(10), 2753–2776. https://doi.org/10.5194/gmd-16-2753-2023

Feng, Z., Leung, L. R., Liu, N., Wang, J., Houze, R. A., Li, J., et al. (2021). A global high-resolution mesoscale convective system database using satellite-derived cloud tops, surface precipitation, and tracking. *Journal of Geophysical Research: Atmospheres*, *126*(8). https://doi.org/10.1029/2020JD034202

Grubišić, V., & Moncrieff, M. W. (2000). Parameterization of convective momentum transport in highly baroclinic conditions. *Journal of the Atmospheric Sciences*, *57*(18), 3035–3049. https://doi.org/10.1175/1520-0469(2000)057<3035:POCMTI>2.0.CO;2

Han, B., Fan, J., Varble, A., Morrison, H., Williams, C. R., Chen, B., et al. (2019). Cloud-resolving model intercomparison of an MC3E squall line case: Part II. Stratiform precipitation properties. *Journal of Geophysical Research: Atmospheres*, *124*(2), 1090–1117. https://doi.org/10.1029/2018JD029596

Hartmann, D. L., Hendon, H. H., & Houze, R. A., Jr. (1984). Some implications of the mesoscale circulations in tropical cloud clusters for large-scale dynamics and climate. *Journal of the Atmospheric Sciences*, *41*(1), 113–121. https://doi.org/10.1175/1520-0469(1984)041<0113:SIOTMC>2.0.CO;2

Hoell, A., Cannon, F., & Barlow, M. (2018). Middle East and Southwest Asia daily precipitation characteristics associated with the Madden–Julian Oscillation during boreal winter. *Journal of Climate*, *31*(21), 8843–8860. https://doi.org/10.1175/JCLI-D-18-0059.1

Houze, R. A. (1989). Observed structure of mesoscale convective systems and implications for large-scale heating. *Quarterly Journal of the Royal Meteorological Society*, *115*(487), 425–461. https://doi.org/10.1002/qj.49711548702

Houze, R. A. (2004). Mesoscale convective systems. *Reviews of Geophysics*, *42*(4), RG4003. https://doi.org/10.1029/2004RG000150

Houze, R. A. (2018). 100 years of research on mesoscale convective systems. *Meteorological Monographs*, *59*. https://doi.org/10.1175/AMSMONOGRAPHS-D-18-0001.1

Houze, R. A., Smull, B. F., & Dodge, P. (1990). Mesoscale organization of springtime rainstorms in Oklahoma. *Monthly Weather Review*, *118*(3), 613–654. https://doi.org/10.1175/1520-0493(1990)118<0613:MOOSRI>2.0.CO;2

Inverarity, G. W., Tennant, W. J., Anton, L., Bowler, N. E., Clayton, A. M., Jardak, M., et al. (2023). Met Office MOGREPS-G initialisation using an ensemble of hybrid four-dimensional ensemble variational (En-4DEnVar) data assimilations. *Quarterly Journal of the Royal Meteorological Society*, *149*(753), 1138–1164. https://doi.org/10.1002/qj.4431

Kassahari, T., & Puri, S. (2020). Eigenmode decomposition in climate models: Variability and predictability analysis. *Journal of Geophysical Research: Atmospheres*, *125*(6), e2019JD031678. https://doi.org/10.1029/2019JD031678

Khouider, B., Goswami, B. B., Phani, R., & Majda, A. J. (2023). A shallow-deep unified stochastic mass flux cumulus parameterization in the single column Community Climate Model. *Journal of Advances in Modeling Earth Systems*, *15*(11), e2022MS003391. https://doi.org/10.1029/2022MS003391

Khouider, B., & Moncrieff, M. W. (2015). Organized convection parameterization for the ITCZ. *Journal of the Atmospheric Sciences*, *72*(8), 3073–3096. https://doi.org/10.1175/JAS-D-15-0006.1.2

Khouider, B., St-Cyr, A., Majda, A. J., & Tribbia, J. (2011). The MJO and convectively coupled waves in a coarse-resolution GCM with a simple multicloud parameterization. *Journal of the Atmospheric Sciences*, *68*(2), 240–264. https://doi.org/10.1175/2010JAS3443.1

Kooperman, G. J., Pritchard, M. S., & Somerville, R. C. J. (2014). The response of US summer rainfall to quadrupled CO2 climate change in conventional and superparameterized versions of the NCAR community atmosphere model. *Journal of Advances in Modeling Earth Systems*, *6*(3), 859–882. https://doi.org/10.1002/2014MS000306

Lauer, A., Bock, L., Hassler, B., Schröder, M., & Stengel, M. (2023). Cloud climatologies from global climate models—A comparison of CMIP5 and CMIP6 models with satellite data. *Journal of Climate*, *36*(2), 281–311. https://doi.org/10.1175/JCLI-D-22-0181.1

Lavender, S. L., Stirling, A. J., Whitall, M., Stratton, R., Daleu, C. L., Plant, R. S., et al. (2024). The use of idealised experiments in testing a new convective parameterization: Performance of CoMorph-A. To appear in. *Quarterly Journal of the Royal Meteorological Society*, *150*(760), 1581–1600. https://doi.org/10.1002/qj.4660

Leary, C. A., & Houze, R. A. (1979). Melting and evaporation of hydrometeors in precipitation from the anvil clouds of deep tropical convection. *Journal of the Atmospheric Sciences*, *36*(4), 669–679. https://doi.org/10.1175/1520-0469(1979)036<0669:MAEOHI>2.0.CO;2

Liebmann, B., & Smith, C. A. (1996). Description of a complete (interpolated) outgoing longwave radiation dataset. *Bulletin of the American Meteorological Society*, *77*, 1275–1277. https://doi.org/10.1175/1520-0477-77.1.fmi

Liu, C., & Moncrieff, M. W. (2017). Shear-parallel mesoscale convective systems in a moist low-inhibition Mei-Yu front environment. *Journal of the Atmospheric Sciences*, *74*(12), 4213–4228. https://doi.org/10.1175/JAS-D-17-0121.1

Lock, A. P., Whitall, M., Stirling, A. J., Williams, K. D., Lavender, S. L., Morcrette, C., et al. (2024). The performance of the CoMorph-A convection package in global simulations with the Met Office Unified Model. *Quarterly Journal of the Royal Meteorological Society*, *150*(763), 3527–3543. https://doi.org/10.1002/qj.4781

Majda, A. J., & Shefter, M. G. (2001). Models for stratiform instability and convectively coupled waves. *Journal of the Atmospheric Sciences*, *58*(12), 1567–1584. https://doi.org/10.1175/1520-0469(2001)058<1567:mfsiac>2.0.co;2

Mapes, B. E. (2000). Convective inhibition, subgrid-scale triggering energy, and stratiform instability in a toy tropical wave model. *Journal of the Atmospheric Sciences*, *57*(10), 1515–1535. https://doi.org/10.1175/1520-0469(2000)057<1515:CISSTE>2.0.CO;2

Moncrieff, M. W. (1981). A theory of organized steady convection and its transport properties. *Quarterly Journal of the Royal Meteorological Society*, *107*(451), 29–50. https://doi.org/10.1002/qj.49710745103

Moncrieff, M. W. (1992). Organized convective systems: Archetypal dynamic-models, mass and momentum flux theory, and parametrization. *Quarterly Journal of the Royal Meteorological Society*, *118*(507), 819–850. https://doi.org/10.1002/qj.49711850703

Moncrieff, M. W. (2019). Toward a dynamical foundation for organized convection parameterization in GCMs. *Geophysical Research Letters*, *46*(14), 14103–14108. https://doi.org/10.1029/2019GL085316

Moncrieff, M. W., & Liu, C. (2006). Representing convective organization in prediction models by a hybrid strategy. *Journal of the Atmospheric Sciences*, *63*(12), 3404–3420. https://doi.org/10.1175/JAS3812.1

Moncrieff, M. W., Liu, C., & Bogenschutz, P. (2017). Simulation, modeling, and dynamically based parameterization of organized tropical convection for global climate models. *Journal of the Atmospheric Sciences*, *74*(5), 1363–1380. https://doi.org/10.1175/JAS-D-16-0166.1

Muetzelfeldt, M. R., Plant, R. S., Christensen, H. M., Zhang, Z., Woollings, T., Feng, Z., & Li, P. (2025). Environmental conditions affecting global mesoscale convective system occurrence. *Journal of the Atmospheric Sciences*, *82*(2), 391–407. https://doi.org/10.1175/JAS-D-24-0058.1

Prein, A. F., Liu, C., Ikeda, K., Bullock, R., Rasmussen, R. M., Holland, G. J., & Clark, M. (2020). Simulating North American mesoscale convective systems with a convection-permitting climate model. *Climate Dynamics*, *55*(1), 95–110. https://doi.org/10.1007/s00382-017-3993-2

Rushley, S. S., Kang, D., Kim, D., An, S.-I., & Wang, T. (2023). MJO in different orbital regimes: Role of the mean state on the MJO's amplitude during boreal winter. *Journal of Climate*, *36*(13), 1–41. https://doi.org/10.1175/JCLI-D-22-0725.1

Schumacher, C., Houze, R. A., & Kraucunas, I. (2004). The tropical dynamical response to latent heating estimates derived from the TRMM precipitation radar. *Journal of the Atmospheric Sciences*, *61*(12), 1341–1358. https://doi.org/10.1175/1520-0469(2004)061<1341:TTDRTL>2.0.CO;2

Schumacher, R. S., & Rasmussen, K. L. (2020). The formation, character and changing nature of mesoscale convective systems. *Nature Reviews Earth & Environment*, *1*(6), 300–314. https://doi.org/10.1038/s43017-020-0057-7

Skamarock, W. C. (2004). Evaluating mesoscale NWP models using kinetic energy spectra. *Monthly Weather Review*, *132*(12), 3019–3032. https://doi.org/10.1175/MWR2830.1

Varble, A., Zipser, E. J., Fridlind, A. M., Zhu, P., Ackerman, A. S., Chaboureau, J.-P., et al. (2014a). Evaluation of cloud-resolving and limited area model intercomparison simulations using TWP-ICE observations: 1. Deep convective updraft properties. *Journal of Geophysical Research: Atmospheres*, *119*(24), 13891–13918. https://doi.org/10.1002/2013JD021371

Varble, A., Zipser, E. J., Fridlind, A. M., Zhu, P., Ackerman, A. S., Chaboureau, J.-P., et al. (2014b). Evaluation of cloud-resolving and limited area model intercomparison simulations using TWP-ICE observations: 2. Precipitation microphysics. *Journal of Geophysical Research: Atmospheres*, *119*(24), 13919–13945. https://doi.org/10.1002/2013JD021372

Waliser, D., Sperber, K., Hendon, H., Kim, D., Maloney, E., Wheeler, M., et al. (2009). MJO simulation diagnostics. *Journal of Climate*, *22*, 3006–3030. https://doi.org/10.1175/2008JCLI2731.1

Walters, D., Baran, A. J., Boutle, I., Brooks, M., Earnshaw, P., Edwards, J., et al. (2019). The Met Office Unified Model global atmosphere 7.0/7.1 and JULES global land 7.0 configurations. *Geoscientific Model Development*, *12*(5), 1909–1963. https://doi.org/10.5194/gmd-12-1909-2019

Wheeler, M. C., & Hendon, H. H. (2004). An all-season real-time multivariate MJO index: Development of an index for monitoring and prediction. *Monthly Weather Review*, *132*(8), 1917–1932. https://doi.org/10.1175/1520-0493(2004)132<1917:AARMMI>2.0.CO;2

Whitall, M., Stirling, A., Lock, A., Lavender, S., Stratton, R., & Matsubayashi, K. (2022). The CoMorph convection scheme. *UM Documentation Paper 043*.

Yang, G.-Y., & Slingo, J. (2001). The diurnal cycle in the tropics. *Monthly Weather Review*, *129*(4), 784–801. https://doi.org/10.1175/1520-0493(2001)129<0784:TDCITT>2.0.CO;2

Zhang, G. J., & McFarlane, N. A. (1995). Sensitivity of climate simulations to the parameterization of cumulus convection in the Canadian climate centre general circulation model. *Atmosphere-Ocean*, *33*(3), 407–446. https://doi.org/10.1080/07055900.1995.9649539

Zhang, Z., Christensen, H. M., Muetzelfeldt, M. R., Woollings, T., Plant, R. S., Stirling, A. J., et al. (2024). Organized convection parameterization source code for submission: "Advancing organized convection representation in the unified model: Implementing and enhancing multiscale coherent structure parameterization" to Journal of Advances in Modeling Earth Systems [Software]. *Zenodo*. https://doi.org/10.5281/zenodo.13683478

Zhang, Z., Christensen, H. M., Muetzelfeldt, M. R., Woollings, T., Plant, R. S., Stirling, A. J., et al. (2025). Supporting datasets for submission: "Advancing organized convection representation in the unified model: Implementing and enhancing multiscale coherent structure parameterization" to Journal of Advances in Modeling Earth Systems [Dataset]. *Zenodo*. https://doi.org/10.5281/zenodo.14837977

Zhang, Z., Varble, A., Feng, Z., Hardin, J., & Zipser, E. (2021). Growth of mesoscale convective systems in observations and a seasonal convection-permitting simulation over Argentina. *Monthly Weather Review*, *149*(10), 3469–3490. https://doi.org/10.1175/MWR-D-20-0411.1

Zhang, Z., Varble, A., Feng, Z., Marquis, J., Hardin, J., & Zipser, E. (2024). Dependencies of simulated convective cell and system growth biases on atmospheric instability and model resolution. *Journal of Geophysical Research: Atmospheres*, *129*(22), e2024JD04190. https://doi.org/10.1029/2024JD041090